Development and evaluation of a subject-specific lower limb model with an eleven-degrees-of-freedom natural knee model using magnetic resonance and biplanar x-ray imaging during a quasi-static lunge

Dejtiar, David Leandro; Dzialo, Christine Mary; Pedersen, Peter Heide; Jensen, Kenneth Krogh ; Fleron, Martin Kokholm; Andersen, Michael Skipper

Published in:
Journal of Biomechanical Engineering

DOI (link to publication from Publisher):
10.1115/1.4044245

Publication date:
2020

Document Version
Accepted author manuscript, peer reviewed version

[redacted]

Journal of Biomechanical Engineering. Received January 15, 2019;
Accepted manuscript posted July 18, 2019. doi:10.1115/1.4044245

Development and evaluation of a subject-specific lower limb model with an 11 DOF natural knee model using MRI and EOS during a quasi-static lunge

David Leandro Dejtiar
Department of Materials and Production
Aalborg University, Fibigestræde 16, DK-9220 Aalborg, Denmark
dld@mp.aau.dk

Christine Mary Dzialo
Department of Materials and Production
Aalborg University, Fibigestræde 16, DK-9220 Aalborg, Denmark
Anybody Technology A/S
Niels Jernes Vej 10, DK-9220 Aalborg, Denmark
cmd@anybodytech.com

Peter Heide Pedersen
Department of Orthopedic Surgery
Aalborg University Hospital, Hobrovej 18-22, DK-9000 Aalborg, Denmark
php@rn.dk

Kenneth Krogh Jensen
Department of Radiology
Aalborg University Hospital, Hobrovej 18-22, DK-9000 Aalborg, Denmark
kekj@rn.dk

Martin Kokholm Fleron
Department of Health Science and Technology
Aalborg University, Frederik Bajers Vej 7, DK-9220 Aalborg, Denmark
martinfleron@gmail.com

Michael Skipper Andersen
Department of Materials and Production
Aalborg University, Fibigestræde 16, DK-9220 Aalborg, Denmark
msa@mp.aau.dk

ABSTRACT

Musculoskeletal models can be used to study the muscle, ligament, and joint mechanics of natural knees. However, models that both capture subject-specific geometry and contain a detailed joint model do not currently exist. This study aims to first develop magnetic resonance image (MRI)-based subject-specific models with a detailed natural knee joint capable of simultaneously estimating in vivo ligament, muscle, tibiofemoral (TF), and patellofemoral (PF) joint contact forces and secondary joint kinematics. Then, to evaluate the models, predicted secondary joint kinematics were compared to in vivo joint kinematics extracted from biplanar X-ray images (acquired using slot scanning technology) during a quasi-static lunge. To construct the models, bone, ligament, and cartilage structures were segmented from MRI scans of four subjects. The models were then used to simulate lunges based on motion capture and force place data. Accurate estimates of TF secondary joint kinematics and PF translations were found: translations were predicted with a mean difference (MD) and standard error (SE) of 2.13±0.22 mm between all trials and measures while rotations had a MD±SE of 8.57±0.63º. Ligament and contact forces were also reported. The presented modeling workflow and resulting knee joint model have potential to aid in the understanding of subject-specific biomechanics and simulating the effects of surgical treatment and or external devices on functional knee mechanics on an individual level.

Journal of Biomechanical Engineering. Received January 15, 2019;
Accepted manuscript posted July 18, 2019. doi:10.1115/1.4044245

Introduction

Joint loads and movements in the musculoskeletal (MS) system are governed by complex interactions between muscles, ligaments, bones, other soft tissues, and external loads. These loads and movements are difficult to measure *in vivo*, therefore, MS models are applied to gain insight into internal kinematics and kinetics. However, many MS models simplify joints [1], i.e. a revolute knee joint, and only recently have studies developed and evaluated complex MS models that estimate knee joint contact forces and secondary joint kinematics [2–8]. An aim to investigate surgical outcomes or interventions for pathologies such as osteoarthritis has driven the development of advanced MS joint models that go beyond idealized joints.

The time-consuming and sometimes unethical processes of identifying parameters required to build musculoskeletal models, steer researchers towards scaling of cadaver-based templates [2,7]. Depending on the amount of subject-specific data available to the user, different levels of personalization can be achieved. For instance, geometric bone can be linearly scaled using anthropometric measurements of the subject [9], or based on bone geometry segmentations from medical images. The muscle origins and insertions can be determined through manual identification [10] or using advanced morphing techniques [2,7]. Although it is known that estimations of internal forces are highly sensitive to musculoskeletal model geometry [11,12], most studies apply linearly scaled models [4–6]. In rare cases, detailed joint models are used [2,7].

Journal of Biomechanical Engineering. Received January 15, 2019;
Accepted manuscript posted July 18, 2019. doi:10.1115/1.4044245

Strong headway has been made on the evaluation and validation of complex subject-specific musculoskeletal models through projects like the "Grand Challenge Competition to Predict in vivo Knee Loads" [13]. This project provides an extensive dataset, including knee contact force measurements obtained from an instrumented total knee arthroplasty (TKA) prosthesis, for researchers to utilize in the development and evaluation of methodologies to estimate knee joint contact forces. Some relevant studies under this framework include Hast and Piazza [4], who used a "dual-joint" paradigm that alternatively predicts muscle forces by inverse dynamics in an idealized knee joint and thereafter analyzes a TKA model with 12 degrees of freedom (DOF) and an elastic foundation contact model by forward dynamic integration in a linearly scaled model. A coupled method, developed by Thelen et al. [6], allows for the concurrent estimation of neuromuscular dynamics and joint mechanics, where a computed muscle control algorithm drives a forward dynamics analysis with an elastic foundation model of a TKA implemented in a linearly scaled model. A similar method simulating muscle and tibiofemoral (TF) contact forces, was developed by Guess et al. [5] using proportional integral derivative (PID) feedback control schemes to track the joint angles during the forward dynamic simulations and compute muscle forces. Their model used subject-specific partial femur, partial tibia, and patella geometries while the rest of the model was linearly scaled. Marra et al. [2] proposed a methodology that simultaneously estimates muscle, ligament, and knee joint contact forces together with internal knee kinematics. This was done by applying the force-dependent kinematics (FDK) method developed by

Journal of Biomechanical Engineering. Received January 15, 2019;
Accepted manuscript posted July 18, 2019. doi:10.1115/1.4044245

Andersen et al. [14] in a model that was morphed from subject-specific femur, tibia, and patella geometries, while the remaining lower limb bones were linearly scaled.

The FDK method is an enhanced inverse dynamic analysis that assumes quasi-static equilibrium around the joints' secondary DOF. According to this method, secondary joint kinematics are computed based on contact models and interactions between ligaments, external loads, and muscle forces in the joint [14].

Although instrumented prostheses provide an extraordinary opportunity to validate models, patients with such devices are rare and the results obtained may not be transferable to natural knees of healthy subjects [5,15,16]. Methodologies developed through MS models of TKA have the potential to be applied in natural knees [7,8,15–18]. However, further validation efforts in subject-specific natural joint modeling must be conducted before generalizing their application.

A different validation approach comparing predicted muscle activation and measured electromyographic (EMG) data has also been taken previously to evaluate models without internal load measurements available [1]. EMG amplitudes represent muscle activation during isometric tasks and correlate well with muscle force [19,20]. However, the EMG signal depends highly on electrode placement and cannot be linearly related to muscle force during dynamic tasks due to complex interactions between muscle forces and EMG signals, therefore allowing only for indirect validation [20,21]. Hence, the best approach to evaluate kinematic model predictions of healthy subjects is with experimental measurements of joint kinematics. Dynamic magnetic resonance imaging (MRI) provides a non-invasive option for measuring in vivo joint kinematics;

nonetheless, these measures must be carefully interpreted due to differences between non-weight- and weight-bearing conditions [15,22–26]. On the other hand, fluoroscopy allows for dynamic measurements of in vivo joint kinematics during weight-bearing conditions [27]. Biplanar X-rays systems, such as EOS™ Imaging, utilize slot-scanning technology allowing to perform static measurements of in vivo joint kinematics during weight-bearing conditions with a low radiation dose [28–31]. It is important to note that kinematic measures obtained from quasi-static biplanar X-ray imaging do not necessarily represent that of dynamic activities [30,31].

The specific goals of this study were to: (1) apply a subject-specific MS modeling workflow based on MRI, motion capture, and force plate data to an enhanced inverse dynamic analysis utilizing the FDK method [2], and (2) evaluate the accuracy of the subject-specific MS models performing a lunge against in vivo kinematic data collected during a quasi-static lunge [30].

Materials and methods

Experimental data

Four healthy male subjects without pre-existing knee injuries (age 38 ± 10 years, body mass 74 ± 7 kg, height 1.82 ± 0.06 m) were recruited for this study. The following procedures were approved by the Scientific Ethical Committee for the Region of Nordjylland and informed consent was obtained prior to data collection.

Journal of Biomechanical Engineering. Received January 15, 2019;
Accepted manuscript posted July 18, 2019. doi:10.1115/1.4044245

Single leg (right) dynamic lunges to roughly 20, 45, 60, and 90 degrees of knee flexion (approximated with the help of a lab technician) were performed by the subjects. Simultaneously, motion from 15 retro-reflective markers was recorded using eight infra-red high-speed cameras (Oqus 300 series) sampling at 100 Hz operated with Qualisys Track Manager v.2.9 (Qualisys, Gothenburg, Sweden). One force platform (AMTI Corp., Watertown, MA) placed under the right foot recorded ground reaction forces and moments concurrently at a frame rate of 2000 Hz. Subjects underwent magnetic resonance imaging (MRI) from pelvis to feet, recorded with a 1.5 T OptimaTM MR450W-70 cm scanner (General Electric Healthcare, Chicago, Illinois, USA) running a T1W-LAVA-XV-IDEAL, coronal plane acquisition. Before the full lower limb scans, 18 MRI-compatible markers were placed on bony landmarks. Detailed right knee acquisitions were taken with a 3T Hdxt upgrade scanner (General Electric Healthcare, Chicago, Illinois, USA) following the Osteoarthritis Initiative (OAI) protocol and adjusted for use of a GE scanner [32,33]. A biplanar X-ray imaging system (EOS Imaging, Paris, France), with slot scanning technology and micro-dose radiation exposure, was used to capture in vivo kinematics of the right knee during quasi-static lunges at approximately 20, 45, 60 and 90 degrees of TF flexion [30]. Biplanar X-ray imaging and motion capture experiments were performed non-simultaneously.

Musculoskeletal model

Template lower limb body model

The subject-specific MS models were developed using the AnyBody Modeling System v.7.1 (AMS, Anybody Technology A/S, Aalborg, Denmark) [34]. The generic human body model from the Anybody Model Repository (AMMR v.1.6) was the basis for the subsequent modifications, consisting of a head, trunk, pelvis, two arms, and two legs. The arms and the left leg were excluded from the model and the right leg was replaced with the Twente Lower Extremity Model (TLEM) 2.0 dataset [10], which includes foot, talus, shank, patella, thigh, and hip segments.

The TLEM 2.0 dataset includes coordinates of bony landmarks, muscle attachments, bony wrapping surfaces, joint centers, and axes of rotation for the lower limbs as well as mass, inertial, and mechanical properties for the muscles. The hip joint was modeled as a spherical joint, while the TF, PF, ankle, and subtalar joints were modeled as revolute joints. The revolute constraints in the TF and PF revolute joints were later released, resulting in a 11 DOF knee joint (as patellar tendon was modeled as rigid). More detail can be found in the FDK-based inverse dynamic analysis section.

Geometric morphing

Subject-specific bone geometries were used to morph the generic TLEM 2.0. dataset bone geometries and corresponding muscle attachments. To achieve this, the full pelvis, right: femur, tibia, talus, foot, and patella, and left femoral head were segmented from the lower limb stack of MRI images using Mimics Research v.19 (Materialise NV, Leuven, Belgium). Segmented 3D geometries were exported as stereolithography (STL) files. Post-processing of the segmented subject-specific bone meshes was performed in

Journal of Biomechanical Engineering. Received January 15, 2019;
Accepted manuscript posted July 18, 2019. doi:10.1115/1.4044245

Meshlab v.2016.12 (ISTI-CNR, Pisa, Italy) [35] to better facilitate the morphing process by approximating the number of vertices in the subject-specific segmented bones (target geometries) to the TLEM 2.0 generic bones (source geometries). The generic bones from the TLEM 2.0 dataset were morphed following an advanced morphing technique, developed by Materialise NV (Leuven, Belgium), to the topology of the subject-specific bones based on the 3D reconstruction method of Reder et al. [36], and evaluated in detail by Pellikaan et al. [37]. This method has been previously used in similar studies with good results [2,7,30]. Geometry-based morphing was not possible for the foot due to an incomplete MRI scan. Therefore, the foot was scaled using an affine transformation based on 16 bony landmarks (see Appendix).

Bony landmarks, joint centers, and axes definition

Surfaces selections were made on the subject-specific bone STLs using 3-Matic Research v.11.0 (Materialise NV, Leuven, Belgium) to define bony landmarks, joint centers, and axes. The bony landmarks were computed with a custom MATLAB v.R2014B (The Mathworks Inc., Natick, MA, USA) script, averaging each selected cluster of triangles on the STL surface. Joint centers and axes were obtained in MATLAB through surface fitting techniques based on the various selections [2,38].

Kinematic analysis

The simulation workflow is divided into three steps: a Multibody Kinematics Optimization (MKO) in a standing trial [39], a MKO in the dynamic trials, and an enhanced inverse dynamic analysis with a FDK method [14].

Journal of Biomechanical Engineering. Received January 15, 2019;
Accepted manuscript posted July 18, 2019. doi:10.1115/1.4044245

In the first step, the position and orientation of each segment were found using the segmented MRI markers and corresponding motion capture markers, during the standing reference trial. The local coordinates of the six cluster markers (superior, lateral, and inferior on the thigh and shank segments) were computed and saved for later use. Subsequently, in a second step, an optimization function that minimized the least-square differences between modeled and experimental markers developed by Andersen et al. [40] was applied to determine the model kinematics during the dynamic motion capture trials. Throughout the kinematic analysis, the pelvis segment had six DOF (three translations and three rotations) relative to the global coordinate system, and all joints were assumed idealized with three DOF at the hip and one DOF at the TF, PF, talocrural, and subtalar joints. The trunk was assumed rigidly attached to the pelvis.

FDK-based inverse dynamic analysis

The resulting optimized model kinematics and experimentally recorded ground reaction forces and moments were used as input to the FDK-based inverse dynamic analysis. In this third step, a second knee model was constructed for implementation into the FDK solver [14]. This knee model removes the existing revolute joint and replaces it with an 11 DOF joint that is stabilized by articular contact forces and ligaments. The 11 DOF knee is made up of five DOF in the PF joint, as the patellar ligament was modeled rigid, and six DOF in the TF joint. From these 11 DOF, only the knee flexion angle was driven by the previous MKO results. The other 10 DOF were free to equilibrate between the muscle, ligament, and contact forces, and the external loads in the FDK solver [14].

Journal of Biomechanical Engineering. Received January 15, 2019;
Accepted manuscript posted July 18, 2019. doi:10.1115/1.4044245

Six residual forces and moments were implemented in the pelvis in substitution for the upper body and excluded left leg.

Ligaments

To restrict and stabilize the TF and PF joints in the natural knee model used in the FDK analysis, ligaments were introduced. Anterior cruciate ligament (ACL), posterior cruciate ligament (PCL), lateral collateral ligament (LCL), medial collateral ligament (MCL), lateral epicondylo-patellar ligament (LEPL), medial PF ligament (MPFL), and lateral transverse ligament (LTL) were segmented from the detailed MRI images in Mimics. Ligament attachment sites were selected on the bone surfaces in 3-Matic and, subsequently, averaged in MATLAB to determine the ligament attachment points. Ligaments were divided into bundles to account for wide origin insertion areas. The ACL was represented by four bundles, PCL three bundles, LCL two bundles, MCL three bundles, MPFL three bundles, LEPL one bundle, and LTL three bundles. The posterior capsule (PC, four bundles) and the anterior lateral ligament (ALL, two bundles) could not be determined from the medical images; therefore they were estimated according to descriptions found in the literature [2,15,41]. Ligaments were characterized by three nonlinear force-displacement regions [42], with the linear strain limit set to 0.03 [43].

The ligament parameters (stiffness and reference strain) of each bundle are shown in Table 3 in the Appendix. These ligament parameter values, originally adapted from Blankevoort et al. [42], were taken from comparable knee models in the literature [2,5,6]. Small adjustments to the ligament reference strains were made to the LCL, MCL and PCL for some subjects to increase the stability of the lateral TF compartment (Table 3).

Journal of Biomechanical Engineering. Received January 15, 2019;
Accepted manuscript posted July 18, 2019. doi:10.1115/1.4044245

Contact model

The articular cartilage from the PF and TF joints was segmented in Mimics and the contact surfaces were selected in 3-Matic. Additionally, the contact surface between the patella and femoral trochlear groove (bone) was also selected in 3-Matic. Four contact sites were then created based on an elastic foundation contact model, one at the PF joint, two at the TF joint (dividing the medial and lateral compartments), and one between the patella and the femoral bony surface. The STL surface meshes were used to compute the contact forces based on an elastic foundation contact model with a pressure module of 9.26 GN/m^3 [2].

Muscle modeling

Muscles were represented by 55 muscle-tendon units modeled using 166 Hill-type one-dimensional string elements running from origin to insertion points along via-points and wrapping surfaces fit to the TLEM 2.0 bone geometries. Three-element Hill type models were used for defining muscle dynamics as proposed by Zajac [19]. Following Klein Horsman et al. [44], the isometric strength of each muscle was determined from the physiological cross-sectional area by multiplication with a factor of 27 N/cm^2. The isometric muscle strength of each muscle unit was further scaled using segment-specific strength scaling factors based on the length and mass of the segment relative to the generic TLEM 2.0 model [45]. Force-length and force-velocity relationships were included in the definition of muscle strength to account for the length- and velocity-dependent effects on the instantaneous muscle strength.

Muscle recruitment

To account for the fact that there are more muscles than DOF in the model, a muscle recruitment problem was set up to minimize a third order polynomial cost function. The objective function minimized cubed muscle activations while ensuring that the dynamic equilibrium equations are fulfilled and that muscles can only pull:

$$\min_{\mathbf{f}} G(\mathbf{f}^{(M)}) = \sum_{i=1}^{n^{(M)}} V_i \left(\frac{f_i^{(M)}}{N_i}\right)^3 \tag{4}$$

$$\mathbf{Cf} = \mathbf{r}$$

$$0 \le f_i^{(M)} \le N_i \qquad i = 1,2, \ldots n^{(M)}$$

The objective function, G, is a function of unknown muscles forces $\mathbf{f}^{(M)}$. V_i is the muscle volume [2] and is introduced to account for sub-divided muscles. The number of muscle branches in the model is $n^{(M)}$, while $f_i^{(M)}$ is the i^{th} muscle force. N_i is the instantaneous muscle strength estimated from the Hill-type muscle model. $\mathbf{C}$ is the coefficient matrix containing all unknown forces, $\mathbf{f}$ is a vector of all unknown forces and $\mathbf{r}$ is a vector that represents the inertia, gyroscopic, and external forces [34].

Tibiofemoral and patellofemoral coordinate systems and measures

Anatomical coordinate systems for tibia and femur were defined following the ISB recommendations as described in Grood and Suntay [46]. The femoral local coordinate system (LCS) origin was situated between the medial and lateral epicondyles. The femoral LCS was orientated with the superior-inferior (SI) axis pointing from the origin to the hip joint center, the medial-lateral (ML) axis perpendicular to the SI-axis and pointing laterally, and the anterior-posterior (AP) axis orthogonal to both and oriented anteriorly

Journal of Biomechanical Engineering. Received January 15, 2019;
Accepted manuscript posted July 18, 2019. doi:10.1115/1.4044245

(Green coordinate system in Fig. 4). The tibial LCS had its origin midway between lateral and medial tibial edges. The orientation of the tibial LCS was defined with the SI-axis running between the ankle joint center and the origin and pointing proximally, the ML-axis was perpendicular to SI-axis and oriented towards the lateral tibial edge, and the AP-axis was orthogonal to both and oriented anteriorly (Red coordinate system in Fig. 4). For the patella, the LCS was defined with its origin placed midway between nodes selected at the most lateral and medial patellar protuberances. The ML-axis ran from the origin to the lateral edge, the SI-axis was defined orthogonal to ML-axis and pointing towards the superior node (located at the middle of the patella's superior surface), and the AP-axis was defined orthogonal to both and oriented anteriorly (Blue coordinate system in Fig. 4).

To compute the respective clinical measures, for the TF joint, non-orthogonal unit base vectors were defined (e_1 along femoral fixed ML-axis, e_3 along tibial fixed SI-axis, and e_2 as the cross product between e_3 and e_1 oriented anteriorly). The rotations followed the right-hand rule about these unit vectors and defined the flexion-extension (FE), abduction-adduction (AA), and internal-external (IE) rotations, respectively. To compute the translations, the vector from the femoral origin to the tibial origin was defined and projected onto each rotation axis.

The patellar kinematics were computed with respect to both femoral and tibial (patellotibial: PT) coordinate systems. Translations were measured as the displacement of the patellar LCS origin relative to both the femoral LCS and tibial LCS. Rotations were measured with Cardan angles in the sequence FE, rotation about the floating axis (AA), and rotation about its long axis (IE) relative to both femoral and tibial coordinate systems.

Experimental measures: biplanar X-ray imaging slot-scanning technology

To evaluate the model performance, previously collected [26] *in vivo* kinematic measures of the TF and PF joints were used. The previously taken images were collected using the EOS biplane X-ray system (Biospace med, France) utilizing slot-scanning technology. These biplanar X-rays were then used to estimate the pose of the femur, tibia, and patella and subsequently compute the relative translations and rotations. First, the bone contours of femur, tibia, and patella were manually marked from each pair of biplanar X-ray images in Mimics. Custom MATLAB code was then used to manually transform the 3D MRI-based bone geometry until its projected contours roughly overlaid the biplane segmented contours. Then, the least-square difference between the biplanar contours and the 3D MRI-based geometry contours was minimized using an iterative closest point (ICP) optimization method [30]. Identical coordinate systems as explained in the preceding section, were created for the 3D bone geometry reconstructions. The AMS was then used to compute the previously defined clinical rotations and translations for 3D bone geometry reconstructions for each of the quasi-static lunge positions (20°, 45°, 60°, and 90°).

Journal of Biomechanical Engineering. Received January 15, 2019;
Accepted manuscript posted July 18, 2019. doi:10.1115/1.4044245

Model evaluation

Seventeen clinical measures (five TF, six PF, and six PT) were extracted from the models at each of the quasi-static lunge TF condition (20°, 45°, 60°, and 90°). The model predictions were evaluated against the experimental measures by plotting the clinical measures (subject mean and standard deviation) as a function of TF flexion. Range of motion (ROM) means and standard deviations were also assessed for each clinical measure for both model predictions and experimental measures. Model predictions were further evaluated against the experimental measurements in terms of mean difference (MD) and standard error (SE) for each clinical measure at each quasi-static lunge TF flexion condition. The difference between the first and second halves of the movement were negligible and, therefore, only the downwards portion of the lunge is shown in the graphs.

Results

Kinematics

TF (Fig. 5), PF (Fig. 6), and PT (Fig. 7) secondary joint kinematics were examined for the experimental measures (circles) and the FDK model predictions (lines). Most FDK model estimates were comparable to the biplane image reconstructions except in the TF abduction-adduction (AA) and patellar rotation measures (Figs. 5-7). The mean kinematic parameters for each quasi-static lunge condition were extracted for the experimental measures (Table 1) and FDK model predictions (Table 2). ROM mean and standard deviation values between the four lunge conditions were also calculated (Tables 1 & 2).

Journal of Biomechanical Engineering. Received January 15, 2019;
Accepted manuscript posted July 18, 2019. doi:10.1115/1.4044245

MD and SE between the experimental measures and model predictions are reported in Table 3. Overall, a MD and SE of 2.13±0.22 mm for translations and 8.57±0.63^o for rotations were predicted for all subjects and measures (Table 3). TF translations resulted in a MD of 0.7±0.23 mm and -0.15±0.48^o for rotations. When investigating the model predicted patellar kinematic rotations, only the PT-AA (MD±SE: -1.10±0.8^o) was comparable to the experimental measures. While, the other PT or PF rotational predictions were not captured well by the FDK model (e.g. PF-FE MD±SE: 16.29±0.79^o or PF-IE MD±SE: -7.71±0.45^o.Fig. 9 and table 3). In addition, PT-AP and PF-SI displacements (MD±SE: 6.30±0.58 mm and 4.58±0.18 mm, respectively) also showed larger mean differences than the other translational measurements.

Joint contact forces

Average femoral contact forces (normalized to body weight) at the medial condyle, lateral condyle, and patellar groove were extracted from 0° to 90° TF flexion and recorded in ISB tibial anatomical coordinate systems [46] (Fig. 8). A clear increase in SI-force (compressive force) was detected for all contact sites with increasing knee flexion. In regards to AP-force, TF contact forces increased and shifted anteriorly, while the PF contact force increased and shifted posteriorly as TF flexion increased. There were no significant changes in ML-force for the TF joint, however the PF ML-force increased and shifted laterally with deeper TF flexion.

Ligament Forces

Ligament force estimates are presented for the major ligaments of the TF joint (ACL, PCL, LCL and MCL) and PF joint (LEPL, MPFL, and LTL) in Figures 9 and 10 respectively.

Journal of Biomechanical Engineering. Received January 15, 2019;
Accepted manuscript posted July 18, 2019. doi:10.1115/1.4044245

In the model simulations, the anterior lateral ligament did not contribute to the knee stability and the posterior capsule produced only small forces near full extension, so are not displayed. The ACL, LCL and all PF ligament forces decreased with increasing TF flexion, and the opposite was true for the PCL and MCL. Moreover, despite these trends, there were considerable differences between subjects. Especially for subject-2 (blue in the figures), resulting in larger forces in the ACL, LEPL, LTL and LCL (Figs. 9-10). This may have been due to the larger adduction and internal TF rotations at approximately 80^o of TF flexion compared to the other subjects (Fig. 5).

Discussion

We have constructed four lower-limb MRI-based subject-specific musculoskeletal models that can concurrently predict muscle forces, ligament forces, contact forces, and secondary joint kinematics. The model estimations were evaluated against experimental measures obtained through biplanar X-ray imaging using slot-scanning technology. The specific goals of this study were to: (1) apply a subject-specific MS modeling workflow based on MRI, motion capture, and force plate data to an enhanced inverse dynamic analysis utilizing the FDK method [2], and (2) evaluate the accuracy of the subject-specific MS models performing a lunge against in vivo kinematic data collected during a quasi-static lunge [30].

The TF secondary joint kinematics model estimations were consistent with the in vivo experimental measures and to the model predictions reported by Dzialo et al. [30]. Compared to the moving-axis and revolute models developed by the same authors [30],

Journal of Biomechanical Engineering. Received January 15, 2019;
Accepted manuscript posted July 18, 2019. doi:10.1115/1.4044245

our model performed slightly better in terms of mean difference and standard error for the ML and AP translations of the TF joint. The FDK model showed displacement ROMs (Table 2) of 1.6±0.92 mm (ML) and 12.35±2.82 mm (AP) which was in agreement with the experimental measures and other biplanar fluoroscopic studies (ML 3.25±1.48 mm, 2.5±2.5 mm and 1.5±2 mm, and AP 14.4±5.09 mm, 11.5±4 mm and 16.5±4 mm) [29,30,47], respectively. The same studies reported rotational AA (3.92±2.11^{o}, 2.75±1.5^{o}, and 1.5±3^{o}) and IE (11.84±5.23^{o}, 6±6^{o}, and 10±5^{o}) ROMs which were consistent with our TF rotational predictions (AA of 4.23±1.76^{o} and IE of 7.34±4.85^{o}, Table 2).

The accuracy of the patellar kinematic estimations varied when evaluated with respect to the tibial and femoral coordinate systems. Better agreement was predicted in the ML, SI, and AA (MD±SE: 0.88±0.64 mm, 1.71±0.2 mm and -1.1±0.86^{o}, respectively) when evaluating PT kinematics. While the PF kinematics only showed consistency with the experimental measurements for ML and AP translations (MD±SE: -0.92±0.14 mm and -0.42±0.09 mm, respectively) (Table 3). All PF rotational predictions disagreed with the experimental measures (MD±SE: 16.79±0.79^{o} FE, -7.71±0.45^{o} IE and -10.43±0.33^{o} AA), as well as the PT-FE and IE (MD±SE: 14.73±0.84^{o} and -14.43±0.6^{o} respectively).

Modeling the patellar ligament as a rigid link between two attachment points may be one of the reasons for the errors in the PF and PT kinematics, which may also affect PF contact forces and ligament strains [48]. In the future, modeling the patellar ligament with more bundles, better representing the thick patellar ligament, may help reduce patellar rotations. Another reason that may have influenced the PF kinematics was the segmented articular cartilage (AC), the border between the femoral and the patellar AC

Journal of Biomechanical Engineering. Received January 15, 2019;
Accepted manuscript posted July 18, 2019. doi:10.1115/1.4044245

in the MRI was not always obvious. Which may have introduced inaccuracies in our AC segmentation, potentially affecting the PF contact area and thus how the patella tracks in the PF groove. Moreover, the stiffness, slack length, and reference strain of MPFL, LEPL, and LTL ligaments used were defined based on the literature [2]. Marra et. al. introduced the stiffness to be in the same range of other known ligaments, while defining the reference strain such that the patellar button always ran along the PF groove. Although this choice proved accurate in their model, the geometry of their PF contact was directed by the CAD of the Total Knee Arthroplasty (TKA) [2]. Furthermore, Lenhart et al. [15] used similar ligament parameters and evaluated patellar kinematics during gait against non-weight bearing conditions of similar TF flexion. They suggested that PF behavior was more dependent on cartilage geometries than on ligament properties, supporting the theory that the AC may play a major role in the predicted PF kinematics and consequently in the PF contact forces.

In FDK analysis, the secondary joint kinematics are estimated based on muscle, joint loads, and all elastic forces [14]. Ideally, this would suggest that if the secondary joint kinematics are overall well predicted, then the forces causing these movements should consequently have sufficient accuracy. Marra et al. [2] previously provided evidence of this; and Lenhart et al. [15] using a similar algorithm, achieved secondary joint kinematics consistent with in vivo measurements. Although these previous studies have increased the confidence in MS modeling performance; the predicted kinetics using these methods in natural knees have only been indirectly validated, not guaranteeing correct estimations [49].

Journal of Biomechanical Engineering. Received January 15, 2019;
Accepted manuscript posted July 18, 2019. doi:10.1115/1.4044245

Despite differences in movement, the estimated TF and PF contact forces (Figure 8) are approximately double that of a squat trial modeled with a natural knee [50] of 1.95 BW and 3.78 BW respectively. In addition, Koh et al. (2017) reported the same increasing trend of compressive contact forces relative to knee flexion with extremes occurring at (>85^o) flexion angles. Our results are consistent with findings in Trepczynski et al. [51]; although they modeled TKA, larger PF compressive forces at higher knee flexion angles were also found. The FDK models estimated a peak PF compressive force of 7.47±1.91 BW at 93.2±1.8^o TF flexion, greater than forces reported in the literature [50,51].

PF ligaments were most active during 0 to 50^o of TF flexion (Fig. 10). At higher TF flexion angles, the radii of the femoral condyles in contact with the tibia plateaus are smaller, causing the PF ligaments to shorten. This explains why low PF ligament forces occur during higher TF flexion. Examining the TF ligaments, our results support previous studies [48,50]; suggesting that the PCL helps stabilize AP translations at TF flexion angles greater than 45^o. Interestingly, the mean ACL force from Subject 2 ranged between 100 and 212 N at TF flexion angles greater than 60^o. For this same subject, an increased internal rotation can be observed compared to the other subjects (Fig. 5), suggesting that the ACL acts to prevent internal rotations at high flexion angles.

Nonetheless, this study includes some limitations. First, the biplanar X-ray imaging and motion capture experiments were not conducted simultaneously. This was due to the limited space in the EOS scanner. However, to ensure consistency between the two data collections, the relative foot positions were recorded and ensured during each lunge condition. Additionally, the motion capture lunges were performed dynamically in a slow and controlled form. This allowed us to safely assume quasi-static equilibrium and extract the model kinematics at the same knee flexion angles form the model estimations and biplane X-ray images. Secondly, the MKO used revolute TF and PF joints as input for the FDK analysis which could have introduced inaccuracies in the model kinematics. Dzialo et al. recently demonstrated that predicted secondary joint kinematics differ between moving-axis and revolute joint models, especially with increasing TF flexion [30].

Next, subject-specific ligament parameters were not recorded, so generic ligament parameters were used. In addition, ligament pre-strain had to be tuned for the LCL (+3%) and MCL (+2%) for subject 1 and the PCL (-1%) for subject 3. This was necessary for the FDK residual forces of the model to approach zero and for the model itself to replicate realistic secondary TF joint kinematics and forces when compared to other studies [2,5,6,15]. In the future, we recommend that subject-specific ligament parameter estimates from laxity tests be included in hopes of increasing model accuracy [52]. In addition, ligament wrapping surfaces were not included, which are normally used to prevent the ligaments from penetrating the bone or cartilage surfaces. Without such surfaces this could have affected the ligament moment arms and resulted in altered ligament forces. Moreover, ligaments were represented as nonlinear springs, and unable to simulate the 3D deformable characteristic of ligaments.

Additionally, the models in our study used generic muscle-tendon parameters, utilizing a length-mass scaling approach to scale the muscle strength from the original TLEM 2.0 to the subject-specific models [45]. Ideally this could have been personalized, for example adjusting the muscle model parameters in relation to experimental isometric

Journal of Biomechanical Engineering. Received January 15, 2019;
Accepted manuscript posted July 18, 2019. doi:10.1115/1.4044245

or isokinetic measurements. Such personalization was out of the scope for this project, being such a time-consuming process and requiring maximal effort from the subjects that does not always yield realistic results [53]. Other limitations include the potential for inaccuracies during manual segmentation of bones, articular cartilage, and ligaments; and furthermore, the manual selection of bony landmarks. Therefore, an additional segmentation review of the regions with high priority in terms of muscle attachment sensitivity should be considered in future studies [12]. Additionally, our knee models did not include the menisci, which are important structures to consider when simulating large-load TF kinematics [54]. It should be noted that the biplane image reconstructions required manual operations, which could have increased the predicted error. The accuracy of TF kinematics using these kind of ICP reconstructions has recently been evaluated by Pedersen et al. [52]. They found a mean difference and limits of agreement (LoA) of (0.08 mm and [-1.64 mm, 1.80 mm]) for translations measures and (0.10° and [-0.85°, 1.05°] for rotational measures when comparing reconstructions based on (1) bone marker frames versus (2) the ICP optimization mention above. Furthermore, Pedersen et al. found root mean square errors of 0.88 mm and 0.49° for translational and rotational measures respectively [52].

Extensive studies, requiring hundreds of repeated simulations, would be needed to assess the influence of parameters such as subject-specific geometries or soft tissue mechanical properties. Considering the model simulation time was on average 6 hours per trial, this left a sensitivity analysis out of the scope for this project. The bottleneck in FDK-based inverse dynamics occur when solving for contact, muscle recruitment, and

Journal of Biomechanical Engineering. Received January 15, 2019;
Accepted manuscript posted July 18, 2019. doi:10.1115/1.4044245

muscle wrapping. Fortunately, a recent study has introduced surrogate modeling to FDK-based inverse dynamics, reducing simulation times up to 4.5 min for a single gait cycle [55]. With surrogate modeling, extensive sensitivity studies are more feasible for future researchers.

In conclusion, we have applied a subject-specific multibody musculoskeletal modeling workflow to the natural knee, capable of simultaneously simulating internal TF and PF secondary joint kinematics and contact forces. We have evaluated our subject-specific model estimates against experimental data, extracted from biplane X-ray images, from the same subjects. Good agreement was achieved for all TF secondary joint kinematics and PF translations; however, not for PF or PT rotations. The proposed modeling framework provides a powerful tool to simulate individualized knee mechanics and potentially optimize clinical treatments.

ACKNOWLEDGMENT

We would like to acknowledge Materialise NV for providing the research version of Mimics including the bone morphing methods.

FUNDING

This study was performed under the KNEEMO Initial Training Network, funded by the European Union’s Seventh Framework Programme for research, technological development, and demonstration under Grant Agreement No. 607510 (www.kneemo.eu). This work was also supported by the Sapere Aude program of the Danish Council for Independent Research under grant no. DFF-4184-00018 to M.S.

Journal of Biomechanical Engineering. Received January 15, 2019;
Accepted manuscript posted July 18, 2019. doi:10.1115/1.4044245

Andersen and the Innovation Fund Denmark under the Individualized Osteoarthritis Intervention project.

REFERENCES

[1] Erdemir, A., McLean, S., Herzog, W., and Van den Bogert, A. J., 2007, "Model-Based Estimation of Muscle Forces Exerted during Movements.," Clin. Biomech. (Bristol, Avon), **22**(2), pp. 131–54.

[2] Marra, M. A., Vanheule, V., Fluit, R., Koopman, B. H. F. J. M., Rasmussen, J., Verdonschot, N., and Andersen, M. S., 2015, "A Subject-Specific Musculoskeletal Modeling Framework to Predict In Vivo Mechanics of Total Knee Arthroplasty," J. Biomech. Eng., **137**(2), p. 020904.

[3] Lin, Y. C., Walter, J. P., Banks, S. A., Pandy, M. G., and Fregly, B. J., 2010, "Simultaneous Prediction of Muscle and Contact Forces in the Knee during Gait," J. Biomech., **43**(5), pp. 945–952.

[4] Hast, M. W., and Piazza, S. J., 2013, "Dual-Joint Modeling for Estimation of Total Knee Replacement Contact Forces During Locomotion," J. Biomech. Eng., **135**(2), p. 021013.

[5] Guess, T. M., Stylianou, A. P., and Kia, M., 2014, "Concurrent Prediction of Muscle and Tibiofemoral Contact Forces During Treadmill Gait," J. Biomech. Eng., **136**(2), p. 021032.

[6] Thelen, D. G., Won Choi, K., and Schmitz, A. M., 2014, "Co-Simulation of Neuromuscular Dynamics and Knee Mechanics During Human Walking," J. Biomech. Eng., **136**(2), p. 021033.

[7] Halonen, K. S., Dzialo, C. M., Mannisi, M., Venäläinen, M. S., De Zee, M., and Andersen, M. S., 2017, "Workflow Assessing the Effect of Gait Alterations on Stresses in the Medial Tibial Cartilage - Combined Musculoskeletal Modelling and Finite Element Analysis," Sci. Rep., **7**, p. 17396.

[8] Smith, C. R., Lenhart, R. L., Kaiser, J., Vignos, M. F., and Thelen, D. G., 2015, "Influence of Ligament Properties on Tibiofemoral Mechanics in Walking," J. Knee Surg., **29**(2), pp. 99–106.

[9] Lund, M. E., Andersen, M. S., de Zee, M., and Rasmussen, J., 2015, "Scaling of Musculoskeletal Models from Static and Dynamic Trials," Int. Biomech., **2**(1), pp. 1–11.

[10] Carbone, V., Fluit, R., Pellikaan, P., van der Krogt, M. M., Janssen, D., Damsgaard, M., Vigneron, L., Feilkas, T., Koopman, H. F. J. M., and Verdonschot, N., 2015, "TLEM 2.0 - A Comprehensive Musculoskeletal Geometry Dataset for Subject-Specific Modeling of Lower Extremity," J. Biomech., **48**(5), pp. 734–741.

[11] Gerus, P., Sartori, M., Besier, T. F., Fregly, B. J., Delp, S. L., Banks, S. A., Pandy, M. G., Lima, D. D. D., and Lloyd, D. G., 2013, "Medial Tibiofemoral Contact Forces," J. Biomech., **46**(16), pp. 2778–2786.

[12] Carbone, V., van der Krogt, M. M., Koopman, H. F. J. M., and Verdonschot, N., 2012, "Sensitivity of Subject-Specific Models to Errors in Musculo-Skeletal Geometry," J. Biomech., **45**(14), pp. 2476–2480.

[13] Fregly, B. J., Besier, T. F., Lloyd, D. G., Delp, S. L., Banks, S. A., Pandy, M. G., and

D'Lima, D. D., 2012, "Grand Challenge Competition to Predict in Vivo Knee Loads," J. Orthop. Res., **30**(4), pp. 503–513.

[14] Andersen, M. S., de Zee, M., Damsgaard, M., Nolte, D., and Rasmussen, J., 2017, "Introduction to Force-Dependent Kinematics: Theory and Application to Mandible Modeling," J. Biomech. Eng., **139**(9), p. 091001.

[15] Rachel L. Lenhart, Jarred Kaiser, C. R. S. and D. G. T., 2015, "Prediction And Validation of Load-Dependent Behavior of the Tibiofemoal and Parellofemoral Joints During Movement," Ann Biomed Eng, **43**(11), pp. 2675–2685.

[16] Smith, C. R., Vignos, M. F., Lenhart, R. L., Kaiser, J., and Thelen, D. G., 2016, "The Influence of Component Alignment and Ligament Properties on Tibiofemoral Contact Forces in Total Knee Replacement," J. Biomech. Eng., **138**(2), p. 021017.

[17] Hu, J., Chen, Z., Xin, H., Zhang, Q., and Jin, Z., 2018, "Musculoskeletal Multibody Dynamics Simulation of the Contact Mechanics and Kinematics of a Natural Knee Joint during a Walking Cycle," Proc. Inst. Mech. Eng. Part H J. Eng. Med., **232**(5), pp. 508–519.

[18] Smith, C. R., Brandon, S. C. E., and Thelen, D. G., 2019, "Can Altered Neuromuscular Coordination Restore Soft Tissue Loading Patterns in Anterior Cruciate Ligament and Menisci Deficient Knees during Walking?," J. Biomech., **82**, pp. 124–133.

[19] Zajac, F. E., 1989, "Muscle and Tendon Properties: Models, Scaling, and Application to Biomechanics and Motor Control," CRC Crit. Rev. Biomed. Eng., **17**(CRC Press), pp. 359–411.

[20] Roberts, T. J., and Gabaldón, A. M., 2008, "Interpreting Muscle Function from EMG: Lessons Learned from Direct Measurements of Muscle Force," Integr. Comp. Biol., **48**(2), pp. 312–320.

[21] Meyer, A. J., D'Lima, D. D., Besier, T. F., Lloyd, D. G., Colwell, C. W., and Fregly, B. J., 2013, "Are External Knee Load and EMG Measures Accurate Indicators of Internal Knee Contact Forces during Gait?," J. Orthop. Res., **31**(6), pp. 921–929.

[22] J. Kaiser and A. Monawer and R. Chaudhary and K.M. Johnson, and O. Wieben, and R. K. and D. G. T., 2016, "Accuracy of Model-Based Tracking of Knee Kinematics and Cartilage Contact Measured by Dynamic Volumetric MRI," Med. Eng. Phys., **38**(10), pp. 1131–1135.

[23] Shapiro, L. M., and Gold, G. E., 2012, "MRI of Weight Bearing and Movement," Osteoarthr. Cartil., **20**(2), pp. 69–78.

[24] Westphal, C., Schmitz, A., Reeder, S. B., and Thelen, D. G., 2013, "Load-Dependent Variations in Knee Kinematics Measured with Dynamic MRI," J. Biomech., **46**(12), pp. 2045–2052.

[25] Draper, C. E., Besier, T. F., Fredericson, M., Santos, J. M., Beaupre, G. S., Delp, S. L., and Gold, G. E., 2011, "Differences in Patellofemoral Kinematics between Weight-Bearing and Non-Weight-Bearing Conditions in Patients with Patellofemoral Pain," J. Orthop. Res., **29**(3), pp. 312–317.

[26] Chen, B., Lambrou, T., Offiah, A., Fry, M., and Todd-Pokropek, A., 2011, "Combined MR Imaging towards Subject-Specific Knee Contact Analysis," Vis. Comput., **27**(2), pp. 121–128.

[27] Draper, C. E., Santos, J. M., Kourtis, L. C., Besier, T. F., Fredericson, M., Beaupre, G. S., Gold, G. E., and Delp, S. L., 2008, “Feasibility of Using Real-Time MRI to Measure Joint Kinematics in 1.5T and Open-Bore 0.5T Systems,” J. Magn. Reson. Imaging, **28**, pp. 158–166.

[28] Wybier, M., and Bossard, P., 2013, “Musculoskeletal Imaging in Progress: The EOS Imaging System,” Jt. Bone Spine, **80**(3), pp. 238–243.

[29] Varadarajan, K. M., Gill, T. J., Freiberg, A. A., Rubash, H. E., and Li, G., 2009, “Gender Differences in Trochlear Groove Orientation and Rotational Kinematics of Human Knees,” J. Orthop. Res., **27**(July), pp. 871–878.

[30] Dzialo, C. M., Pedersen, P. H., Simonsen, C. W., Jensen, K. K., de Zee, M., and Andersen, M. S., 2018, “Development and Validation of a Subject-Specific Moving-Axis Tibiofemoral Joint Model Using MRI and EOS Imaging during a Quasi-Static Lunge,” J. Biomech., **72**, pp. 71–80.

[31] Zeighami, A., Dumas, R., Kanhonou, M., Hagemeister, N., Lavoie, F., de Guise, J. A., and Aissaoui, R., 2017, “Tibio-Femoral Joint Contact in Healthy and Osteoarthritic Knees during Quasi-Static Squat: A Bi-Planar X-Ray Analysis,” J. Biomech., **53**(January), pp. 178–184.

[32] Peterfy, C. G., Schneider, E., and Nevitt, M., 2008, “The Osteoarthritis Initiative: Report on the Design Rationale for the Magnetic Resonance Imaging Protocol for the Knee.,” Osteoarthritis Cartilage, **16**(12), pp. 1433–1441.

[33] Balamoody, S., Williams, T. G., Waterton, J. C., Bowes, M., Hodgson, R., Taylor, C. J., and Hutchinson, C. E., 2010, “Comparison of 3T MR Scanners in Regional Cartilage-Thickness Analysis in Osteoarthritis : A Cross-Sectional Multicenter , Multivendor Study,” Arthritis Res. Theraoy, **12**(5), p. R202.

[34] Damsgaard, M., Rasmussen, J., Christensen, S. T., Surma, E., and de Zee, M., 2006, “Analysis of Musculoskeletal Systems in the AnyBody Modeling System,” Simul. Model. Pract. Theory, **14**(8), pp. 1100–1111.

[35] Cignoni, P., Callieri, M., Corsini, M., Dellepiane, M., Ganovelli, F., and Ranzuglia, G., 2008, “MeshLab : An Open-Source Mesh Processing Tool,” Eurographics Ital. Chapter Conf., pp. 129–136.

[36] Redert, A., Kaptein, B., Reinders, M., van den Eelaart, I., and Hendriks, E., 1999, “Extraction of Semantic 3D Models of Human Faces from Stereoscopic Image Sequences,” Acta Stereol., **18**(June 2016), pp. 255–264.

[37] Pellikaan, P., van der Krogt, M. M., Carbone, V., Fluit, R., Vigneron, L. M., Van Deun, J., Verdonschot, N., and Koopman, H. F. J. M., 2014, “Evaluation of a Morphing Based Method to Estimate Muscle Attachment Sites of the Lower Extremity,” J. Biomech., **47**(5), pp. 1144–1150.

[38] Parr, W. C. H., Chatterjee, H. J., and Soligo, C., 2012, “Calculating the Axes of Rotation for the Subtalar and Talocrural Joints Using 3D Bone Reconstructions,” J. Biomech., **45**(6), pp. 1103–1107.

[39] Begon, M., Andersen, M. S., and Dumas, R., 2018, “Multibody Kinematic Optimization for the Estimation of Upper and Lower Limb Human Joint Kinematics: A Systematic Review,” J. Biomech. Eng., **140**(March), p. 030801.

[40] Andersen, M. S., Damsgaard, M., and Rasmussen, J., 2009, “Kinematic Analysis of

Over-Determinate Biomechanical Systems," Comput. Methods Biomech. Biomed. Engin., **12**(4), pp. 371–384.

[41] Kevin B. Shelburne, and Michael R. Torry, A., and Pandy, M. G., 2006, "Contributions of Muscles, Ligaments, and the Ground-Reaction Force to Tibiofemoral Joint Loading During Normal Gait," J. Orthop. Res., **24**(10), pp. 1983–1990.

[42] Blankevoort, L., and Huiskes, R., 1991, "Ligament-Bone Interaction in a Three-Dimensional Model of the Knee," J. Biomech. Eng., **113**(3), p. 263.

[43] Butler, D. L., Kay, M. D., and Stouffer, D. C., 1986, "Comparison of Material Properties in Fascicle-Bone Units From Human Patellar Tendon and Knee Ligaments," J. Biomech., **19**(6), pp. 425–432.

[44] Klein Horsman, M. D., Koopman, H. F. J. M., van der Helm, F. C. T., Prosé, L. P., and Veeger, H. E. J., 2007, "Morphological Muscle and Joint Parameters for Musculoskeletal Modelling of the Lower Extremity," Clin. Biomech., **22**(2), pp. 239–247.

[45] Rasmussen, J., de Zee, M., Damsgaard, M., Christensen, S. T., Marek, C., and Siebertz, K., 2005, "A General Method for Scaling Musculo-Skeletal Models," Int. Symp. Comput. Simul. Biomech. Clevel., **OH**.

[46] Grood, E. S., and Suntay, W. J., 1983, "A Joint Coordinate System for the Clinical Description of Three Dimensional Motions: Application to the Knee," J. Biomech. Eng., **105**(2), pp. 136–144.

[47] Qi, W. and Hosseini, A. and Tsai, T.Y. and Li, J.S. and Rubash, H.E. and Li, G., 2013, "In Vivo Kinematics of the Knee during Weight Bearing High Flexion," J. Biomech., **46**(9), pp. 1576–1582.

[48] Sheehan, F. T., and Drace, J., 2000, "Human Patellar Tendon Strain: A Noninvasive, In Vivo Study.," Clin. Orthop. Relat. Res., **370**, pp. 201–207.

[49] Lund, M. E., De Zee, M., Andersen, M. S., and Rasmussen, J., 2012, "On Validation of Multibody Musculoskeletal Models," Proc. Inst. Mech. Eng. Part H J. Eng. Med., **226**(2), pp. 82–94.

[50] Koh, Y., Nam, J., Son, J., Lee, Y. H., Kim, S., and Kim, S., 2017, "The Effects of Posterior Cruciate Ligament Deficiency on Posterolateral Corner Structures under Gait- and Squat-Loading Conditions," **6**(1), pp. 31–42.

[51] Trepczynski, A., Kutzner, I., Kornaropoulos, E., Taylor, W. R., Duda, G. N., Bergmann, G., and Heller, M. O., 2012, "Patellofemoral Joint Contact Forces during Activities with High Knee Flexion," J. Orthop. Res., **30**(3), pp. 408–415.

[52] Pedersen, D., Vanheule, V., Wirix-speetjens, R., Taylan, O., Delport, H. P., Scheys, L., and Andersen, M. S., 2019, "A Novel Non-Invasive Method for Measuring Knee Joint Laxity in Four Dof : In Vitro Proof-of-Concept and Validation," J. Biomech., **82**, pp. 62–69.

[53] Heinen, F., Lund, M. E., Rasmussen, J., and De Zee, M., 2016, "Muscle-Tendon Unit Scaling Methods of Hill-Type Musculoskeletal Models: An Overview," Proc. Inst. Mech. Eng. Part H J. Eng. Med., **230**(10), pp. 976–984.

[54] Guess, T. M., Thiagarajan, G., Kia, M., and Mishra, M., 2010, "A Subject Specific Multibody Model of the Knee with Menisci," Med. Eng. Phys., **32**(5), pp. 505–515.

Journal of Biomechanical Engineering. Received January 15, 2019;
Accepted manuscript posted July 18, 2019. doi:10.1115/1.4044245

[55] Marra, M. A., Andersen, M. S., Damsgaard, M., Koopman, B. F. J. M., Janssen, D., and Verdonschot, N., 2017, "Evaluation of a Surrogate Contact Model in Force-Dependent Kinematic Simulations of Total Knee Replacement," J. Biomech. Eng., **139**(8), p. 081001.

Figure Captions List

Fig. 1 Illustration of MRI segmentation, morphing, and landmark identification. a) Bone segmentation and 3D reconstruction. b) Morphing of the TLEM 2.0 bones (green) to the segmented bones (blue). c) Ligament segmentation and 3D reconstruction. d) Bony landmark and ligament attachment points selection.

Fig. 2 Overview of the simulation process. Motion capture data from marker trajectories are input to the MKO that computes joint angles. Joint angles and ground reaction forces and moments are input to the FDK-based inverse dynamics model to compute quasi-static equilibrium in the secondary joint DOF to determine muscle forces, ligament and contact forces, and secondary joint kinematics.

Fig. 3 The 11 DOF knee from one subject. The model consists of subject-specific bone, ligament, and cartilage structures.

Fig4. Anatomical coordinate systems. Thigh (green) and shank (red) ISB anatomical coordinate systems. Patellar coordinate system (blue).

Fig. 5 Estimates of TF secondary joint kinematics from FDK models, mean (line) ± deviation (shaded area), compared to experimental biplanar slot X-ray imaging data measures (circles). Subject 1 (red), subject 2 (blue), subject 3 (green), and subject 4 (cyan).

Fig. 6 Estimates of PF secondary joint kinematics from FDK models, mean (line) ± deviation (shaded area), compared to experimental biplanar slot X-ray imaging data measures (circles). Subject 1 (red), subject 2 (blue), subject 3 (green), and subject 4 (cyan).

Fig. 7 Estimates of PT secondary joint kinematics from FDK models, mean (line) ± deviation (shaded area), compared to experimental biplanar slot X-ray imaging data measures (circles). Subject 1 (red), subject 2 (blue), subject 3 (green), and subject 4 (cyan).

Fig. 8 Mean contact forces (lines) and deviations (shaded areas) for each contact site in the tibial ISB anatomical coordinate system. Forces normalized to body weight (BW) and related to knee flexion angle. Subject 1 (red), subject 2 (blue), subject 3 (green), and subject 4 (cyan).

Fig. 9 TF ligaments forces. ACL = anterior cruciate ligament, PCL = posterior cruciate ligament, LCL = lateral collateral ligament and MCL = medial collateral ligament. Subject 1 (red), subject 2 (blue), subject 3 (green), and subject 4 (cyan).

Fig. 10 PF ligaments forces. MPFL = medial PF ligament, LEPL = lateral epicondylopatellar ligament and LTL = lateral transverse ligament. Subject 1 (red), subject 2 (blue), subject 3 (green), and subject 4 (cyan).

Journal of Biomechanical Engineering. Received January 15, 2019;
Accepted manuscript posted July 18, 2019. doi:10.1115/1.4044245

Figure 1.

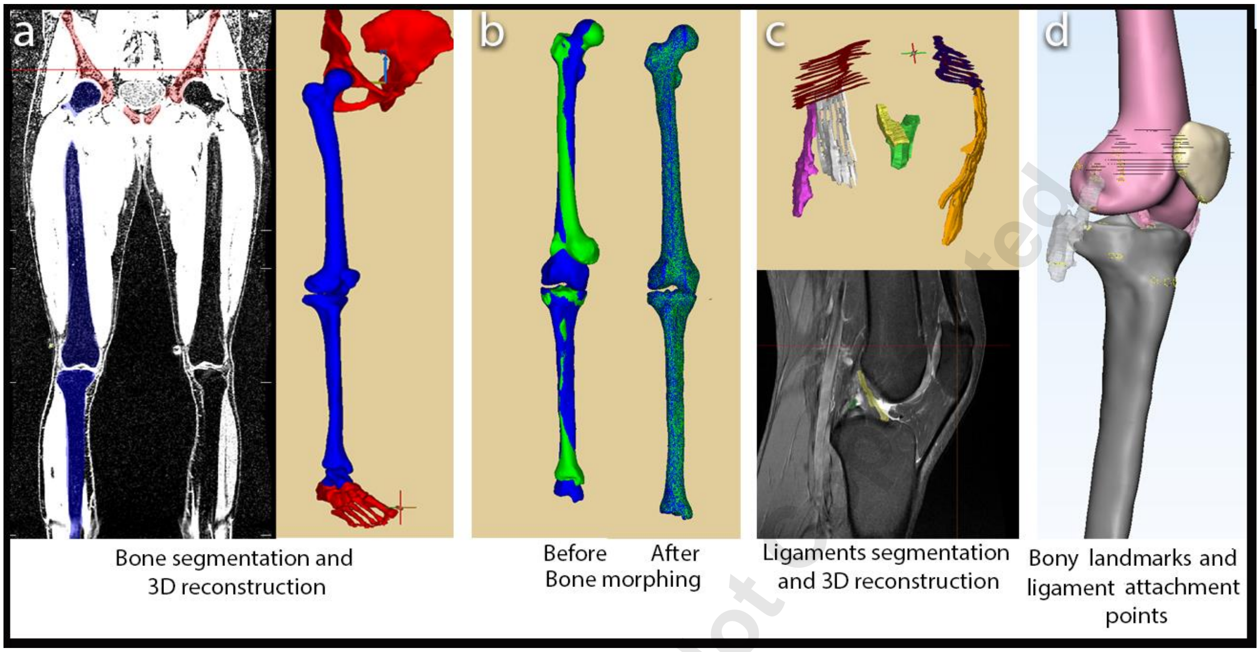

Journal of Biomechanical Engineering. Received January 15, 2019;
Accepted manuscript posted July 18, 2019. doi:10.1115/1.4044245

Figure 2.

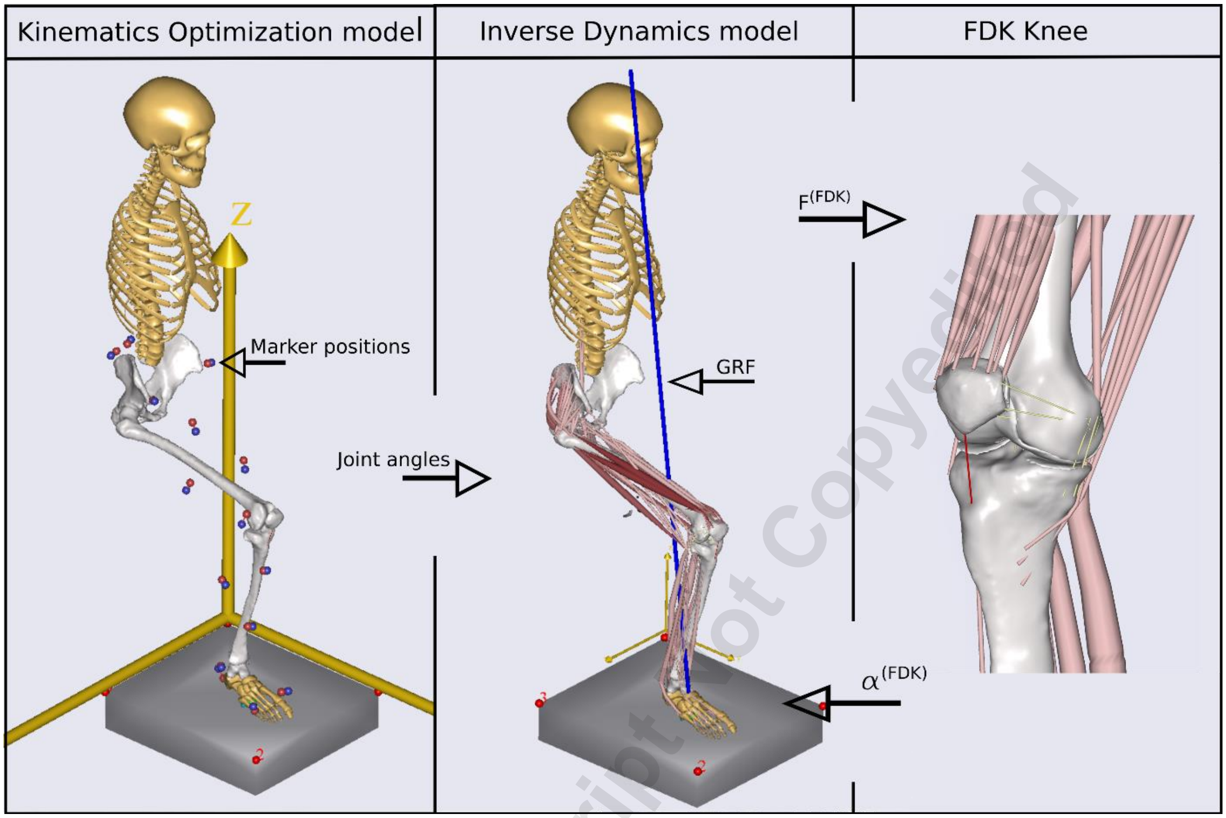

Journal of Biomechanical Engineering. Received January 15, 2019;
Accepted manuscript posted July 18, 2019. doi:10.1115/1.4044245

Figure 3.

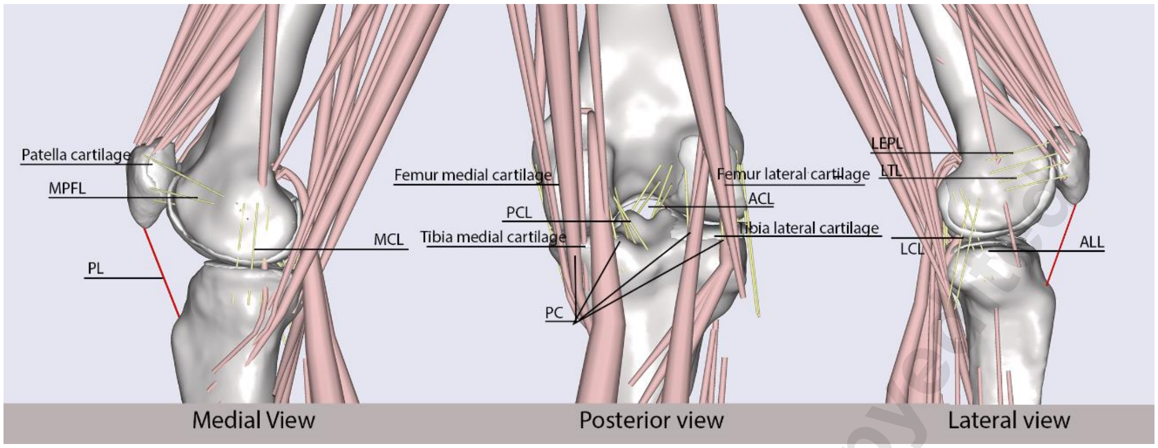

Journal of Biomechanical Engineering. Received January 15, 2019;
Accepted manuscript posted July 18, 2019. doi:10.1115/1.4044245

Figure 4.

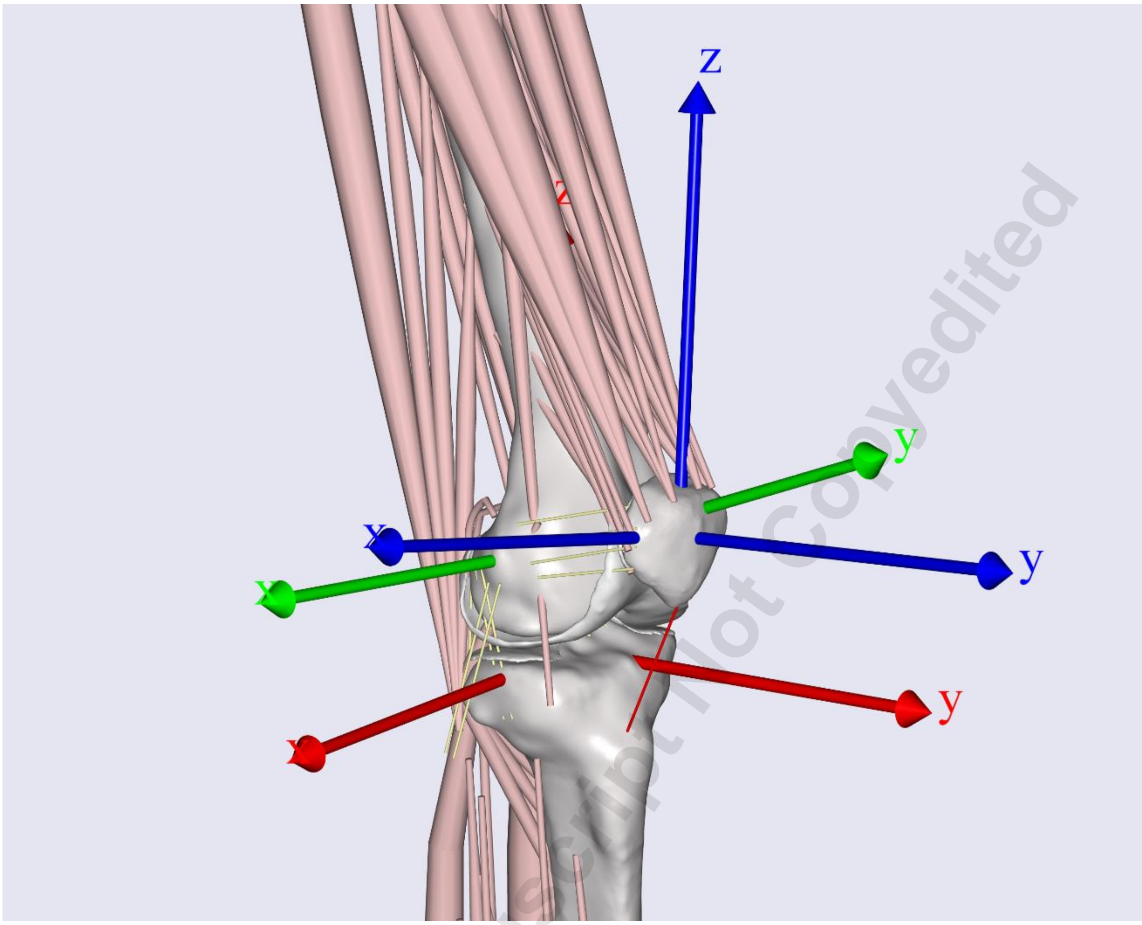

1 Figure 5.

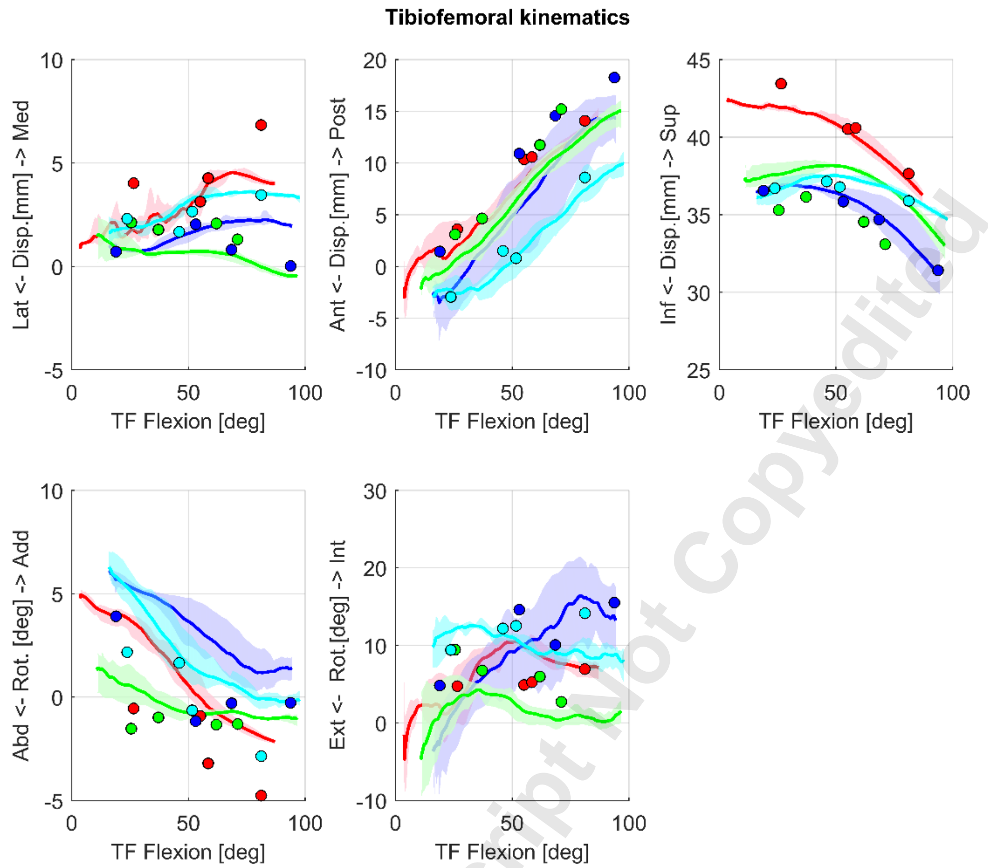
Tibiofemoral kinematics
Lat <- Disp.[mm] -> Med
Ant <- Disp.[mm] -> Post
Inf <- Disp.[mm] -> Sup
Abd <- Rot. [deg] -> Add
Ext <- Rot.[deg] -> Int
TF Flexion [deg]

2

Journal of Biomechanical Engineering. Received January 15, 2019;
Accepted manuscript posted July 18, 2019. doi:10.1115/1.4044245

Figure 6.

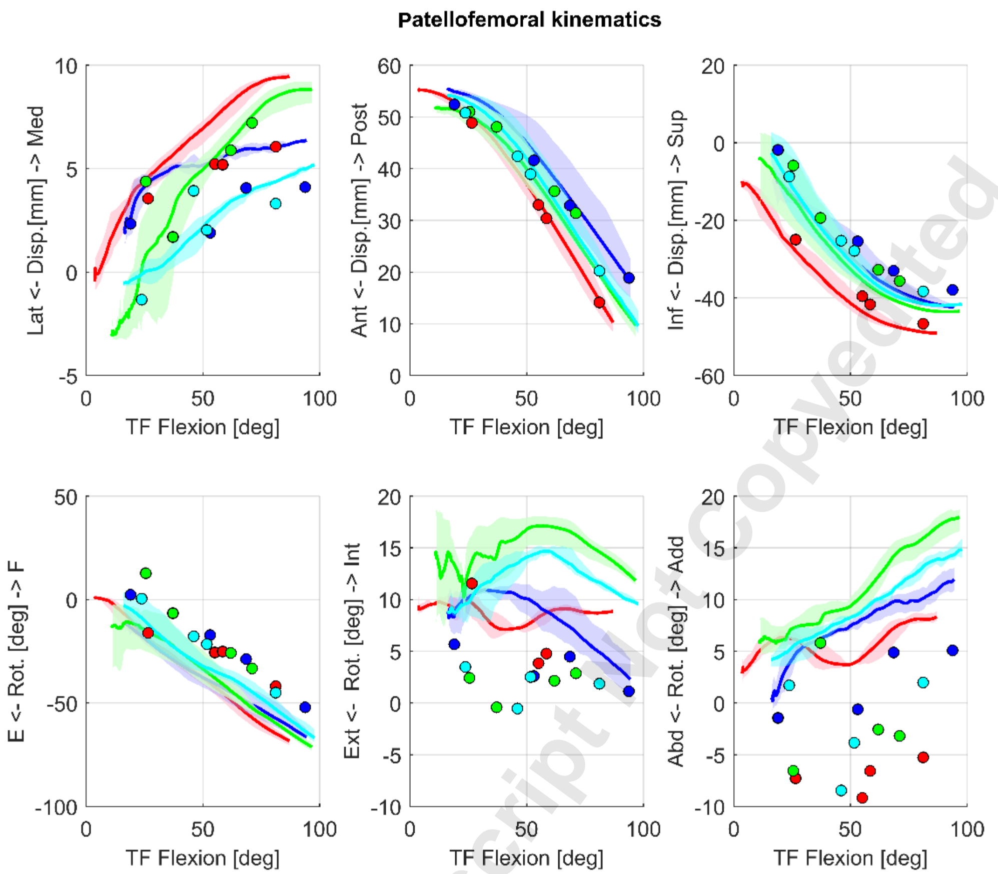

Journal of Biomechanical Engineering. Received January 15, 2019;
Accepted manuscript posted July 18, 2019. doi:10.1115/1.4044245

Figure 7.

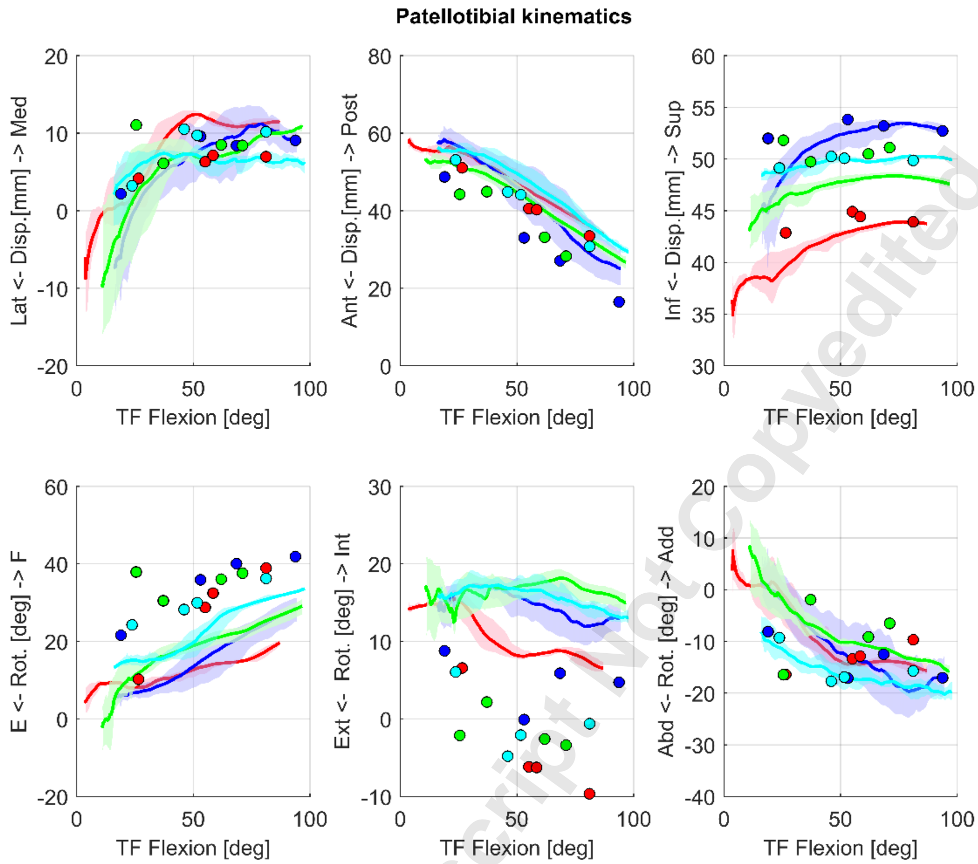

Journal of Biomechanical Engineering. Received January 15, 2019;
Accepted manuscript posted July 18, 2019. doi:10.1115/1.4044245

1 Figure 8.

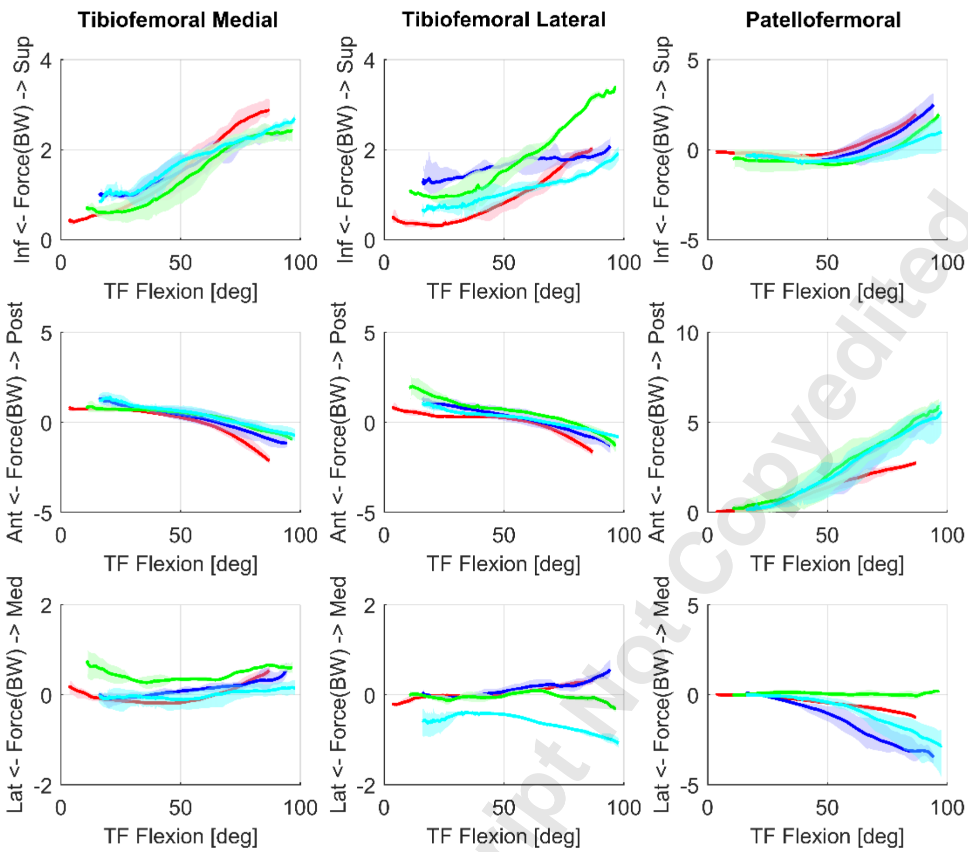

2

Figure 9.

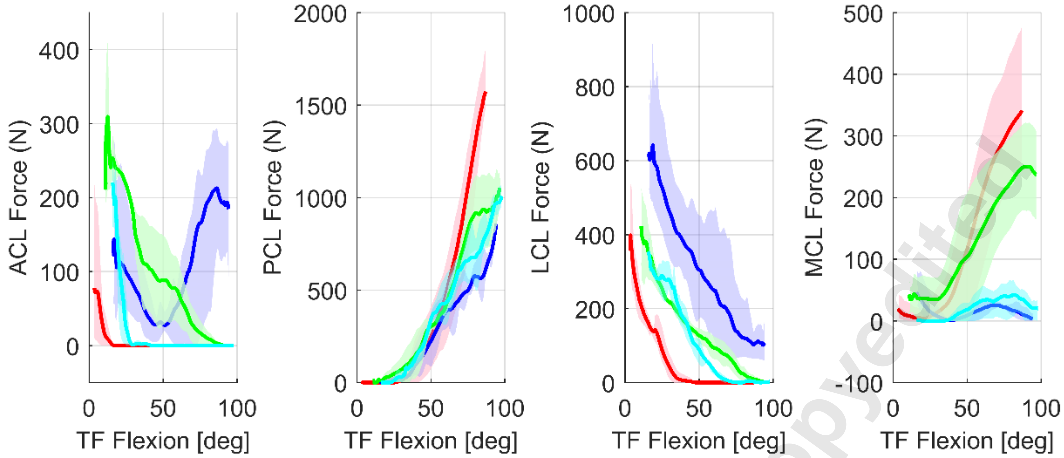
ACL Force (N)
PCL Force (N)
LCL Force (N)
MCL Force (N)
TF Flexion [deg]
TF Flexion [deg]
TF Flexion [deg]
TF Flexion [deg]

Journal of Biomechanical Engineering. Received January 15, 2019;
Accepted manuscript posted July 18, 2019. doi:10.1115/1.4044245

Figure 10.

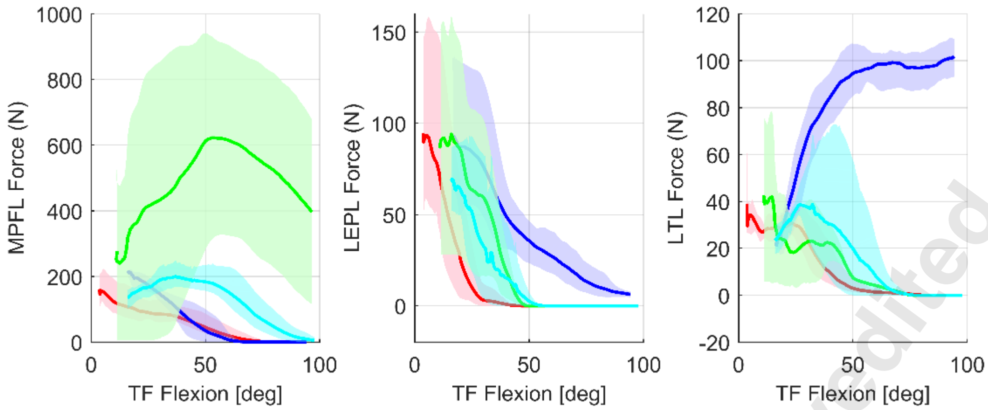

Journal of Biomechanical Engineering. Received January 15, 2019;
Accepted manuscript posted July 18, 2019. doi:10.1115/1.4044245

Table 1. Biplanar slot X-ray imaging experimental measures (mean ± standard deviation) at each quasi-static lunge position and overall ROM for each clinical measure.

Tibiofemoral	Translations (mm)			Rotations (°)	
Condition	ML	AP	SI	AA	IE
20° Flexion	2.29 ± 1.18	1.30 ± 2.57	38.00 ± 3.19	1.01 ± 2.16	7.11 ± 2.32
45° Flexion	2.16 ± 0.58	6.86 ± 3.94	37.42 ± 1.86	-0.35 ± 1.16	9.63 ± 3.93
60° Flexion	2.45 ± 1.24	9.43 ± 5.19	36.66 ± 2.44	-1.37 ± 1.13	8.47 ± 2.98
90° Flexion	2.91 ± 2.58	14.05 ± 3.49	34.51 ± 2.42	-2.30 ± 1.69	9.84 ± 5.24
Average (20°- 90°)	2.45 ± 1.60	7.91 ± 6.04	36.65 ± 2.85	-0.75 ± 2.01	8.76 ± 3.94
ROM	2.08 ± 1.05	12.75 ± 2.43	3.82 ± 1.79	3.72 ± 1.87	6.09 ± 3.10

Patellotibial	Translations (mm)			Rotations (°)		
Condition	ML	AP	SI	FE	IE	AA
20° Flexion	5.16 ± 3.48	49.29 ± 3.30	48.96 ± 3.69	23.52 ± 9.86	4.83 ± 4.14	-12.53 ± 3.89
45° Flexion	8.14 ± 1.95	40.85 ± 4.86	49.68 ± 3.17	30.85 ± 3.04	-2.21 ± 3.40	-12.51 ± 6.35
60° Flexion	8.44 ± 0.92	36.18 ± 6.54	49.55 ± 3.19	34.65 ± 3.80	-1.24 ± 4.43	-12.83 ± 2.76
90° Flexion	8.66 ± 1.16	27.27 ± 6.49	49.41 ± 3.32	38.67 ± 2.08	-2.22 ± 5.18	-12.21 ± 4.31
Average (20°- 90°)	7.60 ± 2.56	38.40 ± 9.66	49.40 ± 3.36	31.93 ± 7.90	-0.21 ± 5.24	-12.52 ± 4.52
ROM	5.66 ± 1.84	22.20 ± 6.18	1.77 ± 0.39	17.09 ± 8.11	10.38 ± 3.87	9.67 ± 2.92

Patellofemoral	Translations (mm)			Rotations (°)		
Condition	ML	AP	SI	FE	IE	AA
20° Flexion	2.24 ± 2.19	50.77 ± 1.28	-10.33 ± 8.78	-0.11 ± 10.36	5.79 ± 3.53	-3.38 ± 3.70
45° Flexion	3.19 ± 1.47	41.27 ± 5.38	-27.38 ± 7.43	-16.75 ± 6.74	1.38 ± 1.90	-3.10 ± 6.14
60° Flexion	4.30 ± 1.46	34.47 ± 3.18	-33.79 ± 4.98	-25.28 ± 2.57	3.49 ± 1.16	-2.01 ± 4.24
90° Flexion	5.17 ± 1.54	21.16 ± 6.33	-39.62 ± 4.17	-43.01 ± 6.73	1.94 ± 0.62	-0.33 ± 4.09
Average (20°- 90°)	3.72 ± 2.02	36.92 ± 11.68	-27.78 ± 12.80	-21.29 ± 17.04	3.15 ± 2.71	-2.21 ± 4.79
ROM	3.87 ± 1.53	29.60 ± 5.98	29.29 ± 5.12	42.90 ±10.53	5.38 ± 2.51	8.31 ± 3.29

Journal of Biomechanical Engineering. Received January 15, 2019;
Accepted manuscript posted July 18, 2019. doi:10.1115/1.4044245

Table 2. FDK model estimates (mean ± standard deviation) at each quasi-static lunge position and overall ROM for each clinical measure.

Tibiofemoral	Translations (mm)			Rotations (°)	
TF angle	ML	AP	SI	AA	IE
20° Flexion	1.01 ± 0.17	-0.82 ± 1.73	38.20 ± 0.21	3.82 ± 0.20	3.96 ± 2.19
45° Flexion	2.20 ± 0.28	3.89 ± 0.75	38.13 ± 0.09	1.36 ± 0.18	8.19 ± 1.33
60° Flexion	2.48 ± 0.27	7.49 ± 1.03	37.61 ± 0.13	0.53 ± 0.20	8.43 ± 1.35
90° Flexion	2.50 ± 0.19	11.53 ± 1.43	35.37 ± 0.14	-0.38 ± 0.32	7.39 ± 2.85
Average (20°- 90°)	2.05 ± 0.23	5.52 ± 1.23	37.33 ± 0.14	1.33 ± 0.22	7.00 ± 1.93
ROM	1.60 ± 0.92	12.35 ± 2.82	3.19 ± 1.86	4.23 ± 1.76	7.34 ± 4.85

Patellotibial	Translations (mm)			Rotations (°)		
TF angle	ML	AP	SI	FE	IE	AA
20° Flexion	1.17 ± 2.17	55.25 ± 1.79	45.04 ± 1.18	9.21 ± 4.47	14.80 ± 1.66	-3.68 ± 2.80
45° Flexion	7.97 ± 1.24	47.88 ± 0.80	48.15 ± 0.27	15.36 ± 1.07	14.74 ± 1.27	-12.05 ± 1.18
60° Flexion	9.00 ± 1.01	42.21 ± 1.03	48.76 ± 0.18	19.36 ± 1.02	14.13 ± 0.97	-14.60 ± 1.22
90° Flexion	8.73 ± 1.32	33.42 ± 1.52	48.83 ± 0.12	24.87 ± 0.98	13.23 ± 1.49	-15.36 ± 2.48
Average (20°- 90°)	6.72 ± 1.43	44.69 ± 1.29	47.69 ± 0.44	17.20 ± 1.88	14.22 ± 1.35	-11.42 ± 1.92
ROM	8.21 ± 4.82	21.82 ± 6.32	3.97 ± 2.33	15.65 ± 4.57	4.71 ± 1.82	11.85 ± 3.41

Patellofemoral	Translations (mm)			Rotations (°)		
TF angle	ML	AP	SI	FE	IE	AA
20° Flexion	1.47 ± 0.59	52.39 ± 0.33	-15.65 ± 1.19	-14.86 ± 4.36	9.84 ± 1.69	4.75 ± 0.77
45° Flexion	4.51 ± 0.13	42.12 ± 0.15	-32.00 ± 0.18	-33.85 ± 0.93	11.94 ± 1.18	7.28 ± 0.43
60° Flexion	5.67 ± 0.24	34.81 ± 0.18	-38.32 ± 0.16	-42.61 ± 0.88	11.91 ± 0.67	8.84 ± 0.59
90° Flexion	6.92 ± 0.29	20.03 ± 0.15	-43.49 ± 0.12	-59.00 ± 0.87	9.76 ± 0.46	12.02 ± 1.12
Average (20°- 90°)	4.64 ± 0.31	37.34 ± 0.20	-32.36 ± 0.41	-37.58 ± 1.76	10.86 ± 1.00	8.22 ± 0.73
ROM	5.45 ± 1.87	32.36 ± 4.69	27.84 ± 4.58	44.14 ± 6.85	5.20 ± 2.33	7.77 ± 2.36

Journal of Biomechanical Engineering. Received January 15, 2019;
Accepted manuscript posted July 18, 2019. doi:10.1115/1.4044245

Table 3. Mean differences ± standard error between model predictions and biplanar slot X-ray imaging experimental measures.

Tibiofemoral	Translations (mm)			Rotations (°)	
TF angle	ML	AP	SI	AA	IE
20° Flexion	1.28 ± 0.07	2.13 ± 0.77	-0.19 ± 0.10	-2.81 ± 0.09	3.15 ± 0.98
45° Flexion	-0.05 ± 0.12	2.97 ± 0.34	-0.71 ± 0.04	-1.71 ± 0.08	1.44 ± 0.59
60° Flexion	-0.02 ± 0.12	1.93 ± 0.46	-0.95 ± 0.06	-1.89 ± 0.09	0.03 ± 0.60
90° Flexion	0.41 ± 0.08	2.52 ± 0.64	-0.86 ± 0.06	-1.92 ± 0.14	2.45 ± 1.27
Average (20°- 90°)	0.41 ± 0.10	2.39 ± 0.55	-0.68 ± 0.06	-2.08 ± 0.10	1.77 ± 0.86

Patellotibial	Translations (mm)			Rotations (°)		
TF angle	ML	AP	SI	FE	IE	AA
20° Flexion	3.98 ± 0.97	-5.96 ± 0.80	3.92 ± 0.53	14.31 ± 2.00	-9.96 ± 0.74	-8.84 ± 1.25
45° Flexion	0.17 ± 0.56	-7.03 ± 0.36	1.54 ± 0.12	15.49 ± 0.48	-16.94 ± 0.57	-0.46 ± 0.53
60° Flexion	-0.55 ± 0.45	-6.04 ± 0.46	0.80 ± 0.08	15.29 ± 0.45	-15.37 ± 0.43	1.77 ± 0.55
90° Flexion	-0.07 ± 0.59	-6.16 ± 0.68	0.58 ± 0.05	13.81 ± 0.44	-15.45 ± 0.67	3.15 ± 1.11
Average (20°- 90°)	0.88 ± 0.64	-6.30 ± 0.58	1.71 ± 0.20	14.73 ± 0.84	-14.43 ± 0.60	-1.10 ± 0.86

Patellofemoral	Translations (mm)			Rotations (°)		
Angle	ML	AP	SI	FE	IE	AA
20° Flexion	0.77 ± 0.26	-1.63 ± 0.15	5.31 ± 0.53	14.75 ± 1.95	-4.05 ± 0.76	-8.14 ± 0.35
45° Flexion	-1.32 ± 0.06	-0.85 ± 0.07	4.61 ± 0.08	17.10 ± 0.42	-10.56 ± 0.53	-10.38 ± 0.19
60° Flexion	-1.37 ± 0.11	-0.34 ± 0.08	4.52 ± 0.07	17.33 ± 0.39	-8.41 ± 0.3	-10.85 ± 0.26
90° Flexion	-1.75 ± 0.13	1.13 ± 0.07	3.87 ± 0.05	15.99 ± 0.39	-7.82 ± 0.20	-12.36 ± 0.50
Average (20°- 90°)	-0.92 ± 0.14	-0.42 ± 0.09	4.58 ±0.18	16.29 ± 0.79	-7.71 ± 0.45	-10.43 ± 0.33

Journal of Biomechanical Engineering. Received January 15, 2019;
Accepted manuscript posted July 18, 2019. doi:10.1115/1.4044245

APPENDIX

A) Motion Capture

The simulations used in the study were driven by motion capture data that was recorded by an eight infrared high-speed cameras system (Oqus 300 series, Qualisys, Gothenburg, Sweden) which captured 30 retroreflective markers that were placed on bony landmarks (Fig. 1). Each subject performed one static standing trial and 3-4 slow dynamic lunges to approximately 90 degrees of tibiofemoral flexion. In order to drive the model, 17 markers were needed, the rest were excluded. Each of the Markers seen in figure 14 were assigned a label accordingly to the anybody standard using Qualisys Track Manager (QTM). Trials with marker drop outs below 10 percent were gap-filled with a polynomial interpolation function by using the in-built gap-fill trajectory with preview tool in QTM. In trials with marker gaps above 10 percent, the marker was excluded and noted in a spread sheet to remove the marker in the specific trial in AMS.

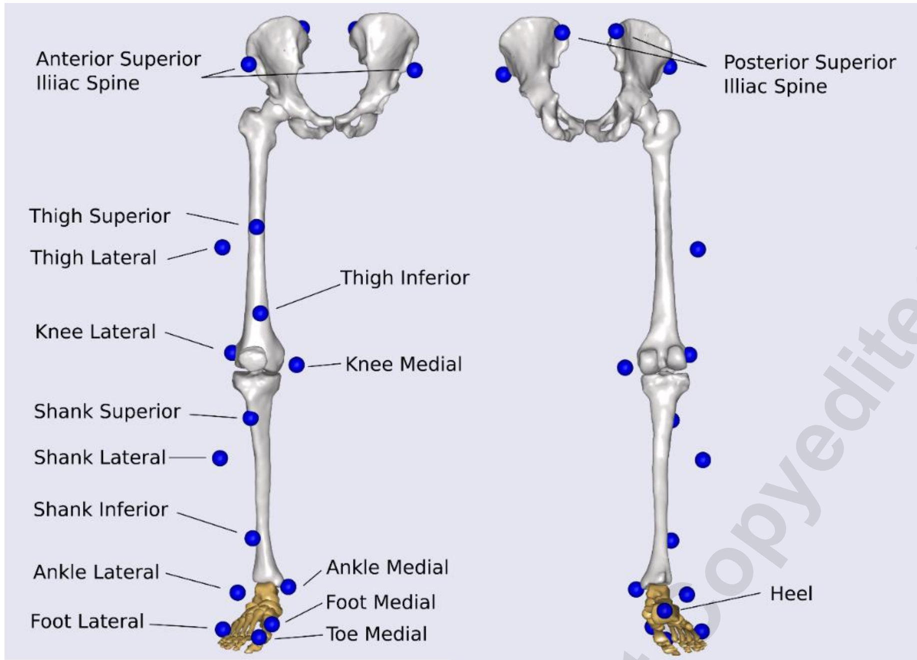

Figure 1: Marker placement for the motion capture trials.

B) **Imaging**

The subject-specific multiscale model is based on MRI's. Subjects underwent two different MRI protocols to gather the necessary data for creating detailed subject-specific models, and biplane X-Ray images to evaluate the simulations' performance.

B.1) Lowerlimb Magnetic Resonance Imaging

In the Lowerlimb MRI scans, the subjects were scanned from pelvis to feet using a 1.5 T OptimaTM MR450W - 70 cm (General Electric Healthcare, Chicago, Illinois, USA) scanner running a T1W-LAVA-XV IDEAL coronal plane scan. The subjects were scanned in three overlapping sections, which were stitched together to make up the lower limb series.

Journal of Biomechanical Engineering. Received January 15, 2019;
Accepted manuscript posted July 18, 2019. doi:10.1115/1.4044245

B.2) Detailed knee Magnetic Resonance Imaging

To create the detailed knee scans the subjects underwent MRI scans with a General Electric 3T (General Electric Healthcare, Chicago, Illinois, USA) scanner running five different protocols: COR PD, SAG 3D, SPGR IDEAL, COR 3D SPGR FS, SAG T1 and SAG PD FS (nomenclature in table 1).

Table 1: Table with MRI Acronyms

MRI Acronyms	Meaning
W	Weighted image
LAVA-XV	Volume interpolated gradient echo
IDEAL	Fat-Water separation
PD	Proton density
FS	Fat suppression
TE	Echo Time
TR	Repetition Time
T1	Short TE and TR times
T2	Longer TE and TR times
SPGR	Spoiled Gradient Echo (produces T1 images in 3D)

B.3) Biplane X-ray images

The biplane X-ray images were creates using EOS™ biplanar X-ray system. The system enables partial or full-body imaging creating continuous, distortion-free images in two orthogonal planes. The subjects performed static lunges at tibiofemoral flexion angles of 0, 20, 45, 60 and 90 degrees. At each angle a pair of orthogonal X-ray images were taken.

Journal of Biomechanical Engineering. Received January 15, 2019;
Accepted manuscript posted July 18, 2019. doi:10.1115/1.4044245

C) Segmentation and morphing

The right foot, talus, tibia, patella, femur, pelvis and the left femur head were manually segmented from the Lowerlimb MRI using Mimics Research 19.0 (Materialise, Belgium). Distal femur, patella, proximal tibia, knee articular cartilage and ligaments were segmented from the detailed MRIs. Each contour is made by creating a mask of the bone through all the MRI slices in two of the three views (Fig. 2, A-B). An interpolation function was used between roughly every three to five slices to speed up the process. The final masks were then converted to 3D objects (Fig. 2, C), which were smoothed and edited to match the bone contours using the inbuilt contour editor toolbox, the finished 3D objects were then exported as STL files.

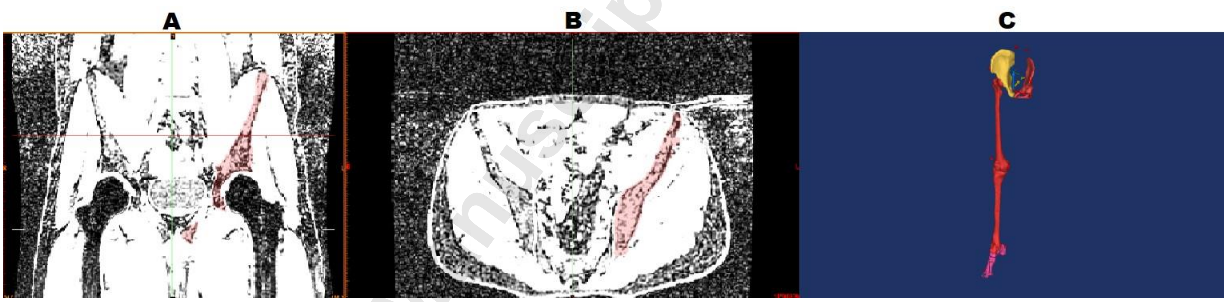

Figure 2: A) MRI Coronal view: Showing a mask of the left pelvis in one slice B) MRI Axial view: Showing a mask of the left pelvis in one slice C) Segmented lower limb 3D View.

In order to match the coordinate system of the Lowerlimb MRI bones to the detailed MRI bones segmented, the Lowerlimb MRI bones were aligned to the detailed bones using either the inertia axis alignment or the point registration tool. The Anybody source bones STLs were then imported into Mimics and morphed to the Lowerlimb's geometry using the 3D Mapping tool, with the parameters shown in table 2.

Table 2: Parameter settings in the morphing tool for the bones.

Journal of Biomechanical Engineering. Received January 15, 2019;
Accepted manuscript posted July 18, 2019. doi:10.1115/1.4044245

	Talus	Tibia	Fibula	Patella	Femur	Pelvis
Tolerance	0.005	0.005	0.05	0.005	0.005	0.05
Percentage	77	99	40	99	99	99
Gamma	0.56	0.90	0.50	0.05	0.05	0.5
Gamma rate	0.3	1.0	0.2	1.0	1.0	0.8
Angle	90	90	20	90	90	60

The incomplete right foot segmentation could not be morphed, and therefore the right foot STL was imported into Meshlab 2016.12 (ISTI-CNR, Italy) where the pick point selection tool was used to select 16 points on the bone surface (Fig. 3). The points where later used in the Anybody Modelling System (AMS, Anybody Technology, Denmark) to scale the foot model through an affine transformation.

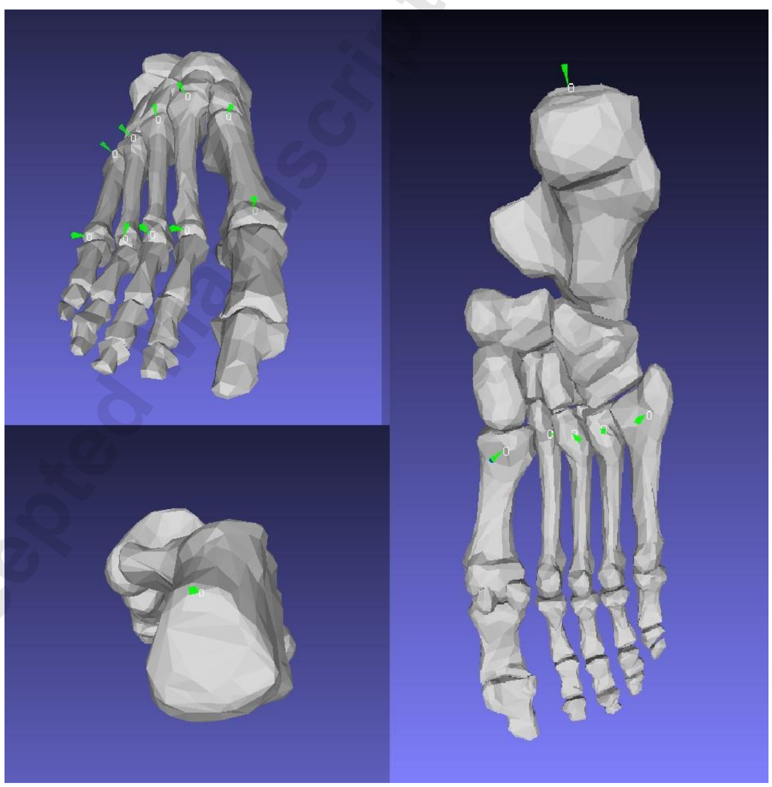

Figure 3: Picked points included in the affine transformations of the foot.

Journal of Biomechanical Engineering. Received January 15, 2019;
Accepted manuscript posted July 18, 2019. doi:10.1115/1.4044245

D) Surface Selections

All segmented objects except the foot were imported into 3-Matic Research v 11.00 (Materialise, Belgium). The lasso area mark tool was used to select bony landmarks, contact surfaces and ligament attachment points on the segmented objects surfaces. The attachment points of the anterior cruciate ligament, medial collateral ligament, lateral collateral ligament, posterior cruciate ligament, medial patellofemoral ligament, lateral epicondylopatellar ligament and lateral transverse ligament were manually selected based on the detailed knee MRIs ligament segmentations and used to select the ligament attachment points on the subjects-specific bone surfaces in 3-Matic. The posterior capsule and anterior lateral ligament attachment sites were selected according to descriptions found in the literature.

E) Ligament parameters

Ligament stiffnesses and reference strains used in the simulations are shown in table 3.

Table 3: Ligament parameters used in the FDK natural knee model.

	Subject 1		Subject 2		Subject 3		Subject 4	
Ligament Bundle	Stiffness (N)	Reference strain (-)	Stiffness (N)	Reference strain (-)	Stiffness (N)	Reference strain (-)	Stiffness (N)	Reference strain (-)
ACL_{lat}	2500	0.06	2500	0.06	2500	0.06	2500	0.06
ACL_{med}	2500	0.06	2500	0.06	2500	0.06	2500	0.06
ACL_{medP}	2500	0.10	2500	0.10	2500	0.10	2500	0.10
ACL_{latP}	2500	0.10	2500	0.10	2500	0.10	2500	0.10
PCL_{med}	6000	-0.02	6000	-0.02	6000	-0.03	6000	-0.02
PCL_{mid}	6000	-0.02	6000	-0.02	6000	-0.03	6000	-0.02
PCL_{lat}	6000	-0.02	6000	-0.02	6000	-0.03	6000	-0.02
MCL_{ant}	2750	0.01	2750	-0.01	2750	-0.01	2750	-0.01

MCL$_{mid}$	2750	0.01	2750	-0.01	2750	-0.01	2750	-0.01
MCL$_{pos}$	2750	0.07	2750	0.05	2750	0.05	2750	0.05
LCL$_{pos}$	3000	0.06	3000	0.03	2000	0.03	3000	0.03
LCL$_{ant}$	3000	0.20	3000	0.17	2000	0.17	3000	0.17
PT	∞	0	∞	0	∞	0	∞	0
ALL$_{pos}$	2000	0.03	2000	0.03	2000	0.03	2000	0.03
ALL$_{ant}$	2000	0.03	2000	0.03	2000	0.03	2000	0.03
PC$_{med}$	1000	0.07	1000	0.07	1000	0.07	1000	0.07
PC$_{midM}$	1000	0.07	1000	0.07	1000	0.07	1000	0.07
PC$_{midL}$	1000	0.07	1000	0.07	1000	0.07	1000	0.07
PC$_{lat}$	1000	0.07	1000	0.07	1000	0.07	1000	0.07
MPFL$_{sup}$	2000	0.12	2000	0.12	2000	0.12	2000	0.12
MPFL$_{mid}$	2000	0.08	2000	0.08	2000	0.08	2000	0.08
MPFL$_{inf}$	2000	0.08	2000	0.08	2000	0.08	2000	0.08
LEPL	1000	0.06	1000	0.06	1000	0.06	1000	0.06
LTL$_{sup}$	1000	0.06	1000	0.06	1000	0.06	1000	0.06
LTL$_{mid}$	1000	0.06	1000	0.06	1000	0.06	1000	0.06
LTL$_{inf}$	1000	0.06	1000	0.06	1000	0.06	1000	0.06